Chapter 1

Introductory Chapter: A Novel Approach to Compute Thermal Conductivity of Complex System

Aamir Shahzad, Syed Irfan Haider, Maogang He and Yan Feng

Additional information is available at the end of the chapter

http://dx.doi.org/10.5772/intechopen.75367

1. Introduction

Thermophysical properties of complex fluids materials (dusty plasmas) have been very actively investigated both experimentally and by computer simulations. These properties describe the physical and chemical behavior of material that remains in terms of fluids formation. Among all of the properties, thermal conductivity is most important; it is an intrinsic property of fluid materials. It is a difficult property from computational point of view because it is sensitive to the internal energy of the system. Its molecular-level observations are becoming more important in dusty plasmas. Dust is abundant in nature. Dust particles coexist in plasmas and then form a complex dusty plasma. Dusty plasmas are ionized gases that contain particulates of condensed matter. Dusty plasmas are of interest as a non-Hamiltonian system of interacting particles and as a means to study generic fundamental physics of self-organization, pattern formation, phase transitions, and scaling. Their discovery has therefore opened new ways of precision investigations in many-particle physics.

2. Dusty plasmas

Dusty plasmas are ionized gases that contain particulates of condensed matter. These particles have different sizes ranging from tens of nanometers to hundreds of microns. The dynamics of these massive charged particles happens at slower timescales than the ordinary plasma ions because charge to mass ratio (e/m) is orders of magnitude smaller that the corresponding (e/m) of either the electrons or ions. They may be in the shape of rods, irregularly shaped pancakes or

spheres. They are made up of dielectric, e.g., SiO_2 *or* Al_2O_3, or conducting materials. Even though the particles are normally solid, they might also be liquid droplets or fluffy ice crystals [1].

3. History of dusty plasmas

Despite almost a century–long history—the first observations of dust in discharges have been reported by Langmuir in 1924. After that, Lyman Spitzer along with Hannes Alfven recognized that dust in the universe was not merely a hindrance to optical observation, but that it was an essential component of the universe. One of the most exciting events in the field of dusty plasmas occurred in early 1980 during the *Voyager 2* flyby of planet Saturn. In 2005, *Cassini* spacecraft took new and improved images of spokes with detail that would provide a better understanding of their origin. In 1992, the European spacecraft *Ulysses* flew by the planet Jupiter and detected the dust particles and measured their masses and impact speed. The current enormous interest in complex plasmas started in the mid-1980s, triggered by laboratory investigation of thermal conductivity of dusty plasmas [2].

4. Types of dusty plasmas

4.1. Weakly vs. strongly coupled dusty plasmas

The vital attention in the investigation of dusty plasmas is whether the particles are in the weakly or strongly coupled state. The description as weakly or strongly coupled denotes the subject of whether the particles average potential energy, due to nearest neighbor interactions, are smaller or larger than their average thermal energy. Coulomb coupling parameter, Γ is defined as the ratio of the interparticle Coulomb potential energy to the (thermal) kinetic energy of the particles:

$$\Gamma = \frac{q^2}{rT} exp\left(\frac{-r}{\lambda_D}\right) \tag{1}$$

where $r = (3/4\pi n)^{1/3}$ is the average interparticle spacing [3].

5. Dusty plasma physics

The brief discussion of the basic principles of dusty plasma physics is given in the following sections.

5.1. Debye shielding

The Debye length is an important physical parameter in a plasma. It provides the distance over which the influence of the electric field of an individual charged particle is felt by other charged particles (such as ions) inside the plasma. The charged particles actually rearrange

themselves in order to shield all electrostatic fields within a Debye distance. In dusty plasmas, the Debye length can be defined as follows [4].

$$\lambda_D = \frac{\lambda_{De}.\lambda_{Di}}{\sqrt{\lambda_{De}^2 + \lambda_{Di}^2}} \tag{2}$$

where $\lambda_{De} = \sqrt{KT_e}/4\pi n_e e^2$ and $\lambda_{Di} = \sqrt{KT_i}/4\pi n_i e^2$ are the Debye lengths associated to electrons and ions, respectively.

5.2. Macroscopic neutrality

Dusty plasmas are characterized as a low-temperature ionized gas whose constituents are electrons, ions, and micron-sized dust particulates. The presence of dust particles (grains) changes the plasma parameters and affects the collective processes in such plasma systems. In particular, the charged dust grains can effectively collect electrons and ions from the background plasma. Thus, in the state of equilibrium, the electron and ion densities are determined by the neutrality condition [5], which is given by

$$en_{i0} - en_{e0} + qn_{d0} = 0 \tag{3}$$

5.3. Inter-grain spacing

In a multicomponent dusty plasma, inter-grain spacing is very important to distinguish between dust in plasma and dusty plasma. Like the dust grain radius, b the inter-grain spacing, r is usually much smaller than the Debye length λ_D. For dust in plasma, $r > \lambda_D$ and the dust particles are completely isolated from their neighbors. For dusty plasmas, $r \leq \lambda_D$ and the dust particles can be considered as massive point particles like multiple-charged negative (or positive) ions in a multispecies plasma where the effect of neighboring particles can be significant.

5.4. Coulomb coupling parameter

Charged dust grains can be either weakly or strong correlated depending on the strength of the Coulomb coupling parameter Eq. (1). When $\Gamma >> 1$, the dust is strongly coupled and this condition is met in several laboratory dusty plasmas, such as dust "plasma crystals". When the dust is weakly coupled, the dispersion relation of waves is not affected by the spatial correlation of the dust grains. A dusty plasma is considered as weakly coupled if $\Gamma << 1$ [6].

5.5. Lattice parameter

In the case of Yukawa interaction, additional screening parameter becomes necessary

$$\kappa = \frac{a_{ws}}{\lambda_D} \tag{4}$$

It is how much effective and protective the shielding out behavior of a single specie against the external or internal stimuli (voltages) that affect inside the plasmas. a_{ws} is the Wigner-Seitz radius which can be estimated as $a_{ws} = (4\pi n/3)^{-1/3}$ [7].

6. The forces on a dust grain in a plasma

The knowledge about various forces acting on dust particles in a plasma is necessary for an understanding of their dynamics and transport.

6.1. Force of gravity, F_g

The dust particle is subject to gravity with a force that is proportional to its mass, but under microgravity condition, it is ignored.

$$\boldsymbol{F}_g = m\boldsymbol{g} = \frac{4}{3}\pi b^3 \rho \boldsymbol{g} \tag{5}$$

where $\boldsymbol{g}$ is the local acceleration due to gravity and ρ is the mass density of the particle [8].

6.2. The electric force, F_e

At a location in the plasma having an electric field $\boldsymbol{E}$, the electric force acting on dust particles of charge q is

$$\boldsymbol{F}_e = q\boldsymbol{E} \tag{6}$$

The electric field is smaller in the bulk of the plasma while it is larger in sheaths next to the plasma wall boundary.

6.3. Neutral drag force, F_n

This force is produced from collisions with the background neutral gas atoms or molecules, and is proportional to the neutral pressure in the vacuum chamber. $\boldsymbol{F}_n$ is given as

$$\boldsymbol{F}_n = Nm_n v^2{}_n \pi b^2 \tag{7}$$

where N is the neutral density, m_n is the mass of the neutral atoms (or molecules), and v_n is the average relative velocity [1].

6.4. Thermophoretic force, F_{th}

This force will be produced due to the temperature gradient in the neutral gas in the plasma, and it's direction is opposite to temperature gradient. This force is given approximately by

$$\boldsymbol{F}_{th} = \frac{16\sqrt{\pi}}{15}\frac{b^2 k_T}{v_{T,n}}\nabla T_n \tag{8}$$

where, $v_{T,n}$ is the thermal speed of the neutral gas, k_T is the translational part of the thermal conductivity, and T_n is the temperature of the neutrals [9].

http://dx.doi.org/10.5772/intechopen.75367

7. Transport properties

7.1. Diffusion coefficient

The diffusion coefficient is the proportionality constant between molar fluxes which is $J_A = -D\Delta C_A$, where Δ is known as gradient operator, D is known as diffusion coefficient ($m^2.\ s^{-1}$), and C_A is the concentration ($mole/m^3$). In the complex (dusty) plasma, the mass, momentum, and energy are transported through dust particles.

7.2. Shear viscosity

Shear viscosity is the measure of force between different layers of fluid. It is the dynamical property of a material such as liquid, solids, gas and dusty plasmas. For liquid, it is familiar thickness, for example, honey and water have different viscosity. The ideal fluid has no resistance between layers in shear stress. The superfluid has zero viscosity at very low temperature. All other liquids have positive viscosity and are said to be viscous.

7.3. Thermal conductivity

The most vital property of the dusty plasma liquids (DPLs) is thermal conductivity and it is due to the internal energy of the molecules. The energy transference of the DPLs and its dependence on the applied external field can be checked by the thermal conductivity. The complete analysis of it is important and necessary for the designing and manufacturing of numerous heat flow devices. The applications in thermo-electronic devices e.g., in semiconductor systems, the phonon thermal conductivity has got a special attention. Due to the atoms' oscillations, phonons of different wavelengths and frequencies are created in solids, and these phonons would disappear when the oscillations stop. Especially, nanotechnology (nanomaterials) requires the accurate calculation of heat transport features [10, 11]. Molecular simulation is recognized as substantial for micro- and nano-scale heat transport phenomena. Furthermore, the new advances require the complete explanations of phase change and the heat, mass transport in micrometer to nanometer scale regimes.

8. Applications

8.1. Dust is a good thing

In the present era, scientists do not consider the dust as an undesirable pollutant; interestingly its positive impacts lead in manufacturing, designing of new devices and direct new developments in material science. In the plasma-chemical mechanism, fine dust particles are also important and having useful properties related to their size and composition. A few of the applications are given below:

1. The efficiency and lifetime of silicon solar cell was increased by the incorporation of amorphous hydrogenated silicon particles (*a-Si:H*) with the nanocrystalline silicon particles which grow in silane plasmas.
2. Thin films of *TiN* in an amorphous Si_3N_4 matrix prepared by PECVD (plasma enhanced chemical vapor deposition) have enormously high hardness and elastic modulus. A thin film coating is applied to materials to improve surface properties.
3. Diamond whiskers made up by etching in radio frequency (*rf*) plasmas improve electron field emission. The reactive ion etching process used in *rf* plasma devices effectively sharpen the micro tips of diamond [12].

8.2. Dust in plasma processing devices (dust is a bad thing)

At first, it was presumed that the semiconductor surfaces were contaminated during handling of the wafers. To lighten the problem, all fabrication steps were done in clean rooms. Yet even with the best state-of-the art clean rooms, semiconductor wafers showed evidence of contamination. It drove out that the surfaces were being soiled by dust particles generated within the processing plasmas. Complex plasma-enhanced chemical reactions take place within these discharges that produce and grow dust particles. Several experimental devices are used to measure the presence and growth of dust particles such as transmission electron microscope (TEM), scanning electron microscope (SEM), laser light scattering etc. Also, theoretical and computational works are directed to investigate the dust formation, growth, charging, and transport.

9. Computational method

9.1. Simulation technique and parameters

Molecular mechanics dynamic simulation (MMDS) is a simplified approach as compared to other techniques. It allows study of molecular ensembles for thousands of atoms. The MMDS technique works as a core on a simple explanation of force between the individual atoms. Here, HPMD approach is implemented to determine the thermal conductivity of CDPs by applying external perturbation which is modeled by using Yukawa potential model use for the explanation of dust particles interacting with one another. Yukawa potential is used for a system of charged particles. While Green-Kubo relation applies to neutral particles,

$$\phi(|\mathbf{r}|) = \frac{q^2}{4\pi\varepsilon_0}\frac{e^{-|\mathbf{r}|/\lambda_D}}{|\mathbf{r}|}, \tag{9}$$

The plasma phase of Yukawa system is representing three dimensionless parameters [7], plasma coupling parameter $\Gamma = (q^2/4\pi\varepsilon_0)(1/a_{ws}K_BT)$, screening strength $\kappa = a_{ws}/\lambda_D$, and $\boldsymbol{F}_e(t) = (F_z)$ is external perturbation with its normalized value $F^* = F_z a_{ws}/J_{QZ}$, where J_{QZ} is thermal heat energy along *z*-axis. The inverse of plasma frequency $\omega_p = (q^2/2\pi\varepsilon_0 m a_{ws}^3)^{1/2}$ characterizes timescale. Simulations are performed for N = 400–14,400 particles in canonical ensemble with PBCs and minimum

image convention of Yukawa particles. In our case, most of the simulations are performed with $N = 400$ particles. The particles are placed in a unit cell with edge length L_x / L_y and the dimensions of square simulation cell are $L_x a_{ws} \times L_y a_{ws}$. The equations of motions for N-Yukawa dust particles are integrated through the predictor–corrector algorithm with simulation time step of $\Delta t = 0.001\omega_p^{-1}$. In our case, the conductivity calculations are reported for a wide range of plasma coupling ($1 \le \Gamma \le 100$) and screening parameters ($1 \le \kappa \le 4$) of 2D Yukawa system at constant normalized external perturbation F^*.

9.2. HNEMD model and thermal conductivity

The Green-Kubo relations (GKRs) are the mathematical terms for transport coefficients in the form of time integral correlation functions. GKR is for hydrodynamic transport coefficient of neutral particles. This formula gives linear response expression for thermal conductivity. It enables our calculations using a time-series record of motion of individual dust particles. For thermal transport coefficient, it is a time integral of the correlation function of the microscopic flux of heat energy and where the required input includes time series for position and velocity of a dust particle.

$$\lambda = \frac{1}{2 K_B A T^2} \int_0^\infty \left\langle \mathbf{J}_Q(t).\mathbf{J}_Q(0) \right\rangle dt, \tag{10}$$

where A represents the area, T denotes the absolute temperature, K_B is Boltzmann's constant. The relation of microscopic heat energy $\mathbf{J}_Q$ is

$$\mathbf{J}_Q A = \sum_{i=1}^{N} \left[\mathrm{E}_i - \frac{1}{2} \sum_{i=j} (\boldsymbol{r}i - \boldsymbol{r}j).\boldsymbol{F}ij \right] . \frac{\boldsymbol{p}_i}{m}, \tag{11}$$

In this equation, $\boldsymbol{r}_{ij} = \boldsymbol{r}_i - \boldsymbol{r}_j$ is the position vector and $\boldsymbol{F}_{ij}$ is the force of interaction on particle i due to j and $\boldsymbol{p}_i$ represents the momentum vector of the i_{th} particle. The energy E_i of particle i is $\mathrm{E}_i = \boldsymbol{p}_i / 2\, m + \frac{1}{2} \Sigma \phi_{ij}$, for $i \neq j$, where ϕ_{ij} is the Yukawa pair potential given in Eq. (9) between particle i and j. According to linear response theory (LRT), the perturbed equations of motion, given by Evans-Gillan [7] is

$$\begin{aligned} \dot{\boldsymbol{r}}_i &= \frac{\boldsymbol{p}_i}{m} \\ \dot{\boldsymbol{p}}_i &= \boldsymbol{F}_i + \mathbf{D}_i(\boldsymbol{r}_i, \boldsymbol{p}_i).\boldsymbol{F}_e(t) \\ \alpha &= \frac{\sum_{i=1}^{N} \left[\boldsymbol{F}_i + \mathbf{D}_i(\boldsymbol{r}_i, \boldsymbol{p}_i).\boldsymbol{F}_e(t) \right] . \boldsymbol{p}_i}{\sum_{i=1}^{N} p_i^2 / m_i} \end{aligned} \tag{12}$$

The tensorial phase space distribution function $\mathbf{D}_i$ ($\boldsymbol{r}_i$, $\boldsymbol{p}_i$) describes the coupling of the system. In the generalization of LRT to a system moving according to non-Hamiltonian dynamics, the response of $\mathbf{D}_i$ ($\boldsymbol{r}_i$, $\boldsymbol{p}_i$) [13] is

$$\langle A(t) \rangle - \langle A(0) \rangle = \beta \int_0^t \left\langle A(t)\, \dot{H}_0(t') \right\rangle dt, \tag{13}$$

where $\dot{H}_0$ is the time derivative of the total energy with respect to field-dependent equation of motion [7] and average brackets denote the statistical average and $\beta = 1/K_B T$.

$$\left\langle \mathbf{J}_Q(t) \right\rangle = \beta A \int_0^t dt \left\langle \mathbf{J}_{Q_z}(t').\mathbf{J}_{Q_z}(0) \right\rangle .\boldsymbol{F}_e(t), \tag{14}$$

When external force is selected parallel to the z-axis $\boldsymbol{F}_e(t) = \boldsymbol{\delta}\ (0, F_z)$, $\boldsymbol{\delta}$ is Dirac delta function. Due to this function, the response of heat energy current is proportional to autocorrelation function itself rather than time integral of this function [14]. The reduced thermal conductivity has the following form:

$$\lambda = \frac{1}{ATF_Z} \int_0^\infty \left\langle \mathbf{J}_{Q_z}(t').\mathbf{J}_{Q_z}(0) \right\rangle dt, \tag{15}$$

Eq. (15) is the basic formula for evaluation of autocorrelation function of heat energy current by a perturbation method. Here it is important to discuss some other factors that are in association with the thermal conductivity i.e., Ewald sum. It is used to measure force, Yukawa potential energy, heat energy current (GKR). In this scheme, original interaction potential is divided into two parts: the long-range part that converges quickly in reciprocal space, a short-range interaction that converges quickly in the real-space part of Ewald-Yukawa potential [15].

10. HNEMD results and discussion

In this section, the thermal conductivity calculations are obtained through homogenous perturbed MD (HPMD) simulations, using Eq. (15), for 2D complex dusty plasma systems. The thermal conductivity is compared here with appropriate frequency normalization in the limit of a suitable equilibrium low value of normalized external perturbation, for an absolute range of plasma coupling ($\Gamma \geq 1$) and screening strength ($\kappa \geq 1$). For 2D case, the thermal conductivity of complex dusty plasmas may be represented as $\lambda_0 = \lambda/nm\omega_p a_{ws}^2$ (normalized by plasma frequency) or $\lambda^* = \lambda/nm\omega_E a_{ws}^2$ (normalized by plasma frequency). This improved HPMD approach to 2D strongly coupled plasmas enables it possible to compute all the possible range of plasma states (Γ, κ) at a constant value of normalized perturbation $F^* = (F_z a_{ws}/J_{QZ})$. In our case, the possible low value of external perturbation is $F^* = 0.02$ at which 2D complex plasma system gives equilibrium thermal conductivity for all plasma state points. Before the external perturbation F^* is switched on, the system is equilibrated using the Gaussian thermostat which generates the canonical ensemble given in Eq. (12). In practice, it is necessary for the MD system to be thermostated for the removal of additional heat that is generated due to work done by the external perturbation F^* [16]. The results obtained through present HPMD approach are shown in **Figures 1–4**, where we have traced the plasma thermal conductivity through a computation of usual Yukawa particles in 2D within the strongly coupled regime for different screening parameters of $\kappa = 1$, 2, 3, and 4, respectively.

http://dx.doi.org/10.5772/intechopen.75367

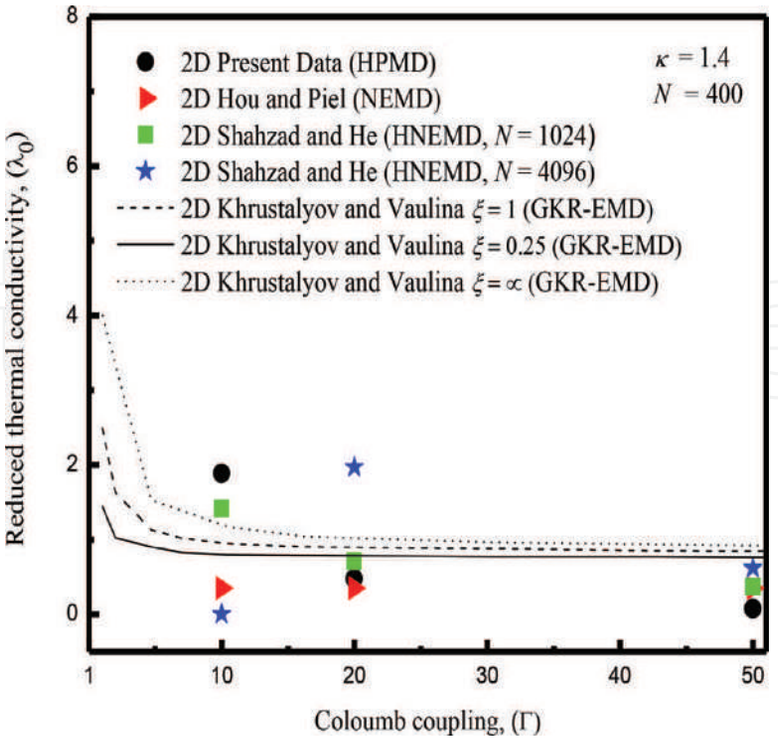

Figure 1. Comparison of results obtained from Yukawa thermal conductivity λ_0 (normalized by ω_p) as a function of plasma coupling Γ ($1 \le \Gamma \le 50$) (system temperature) for SCCDPs at $\kappa = 1.4$.

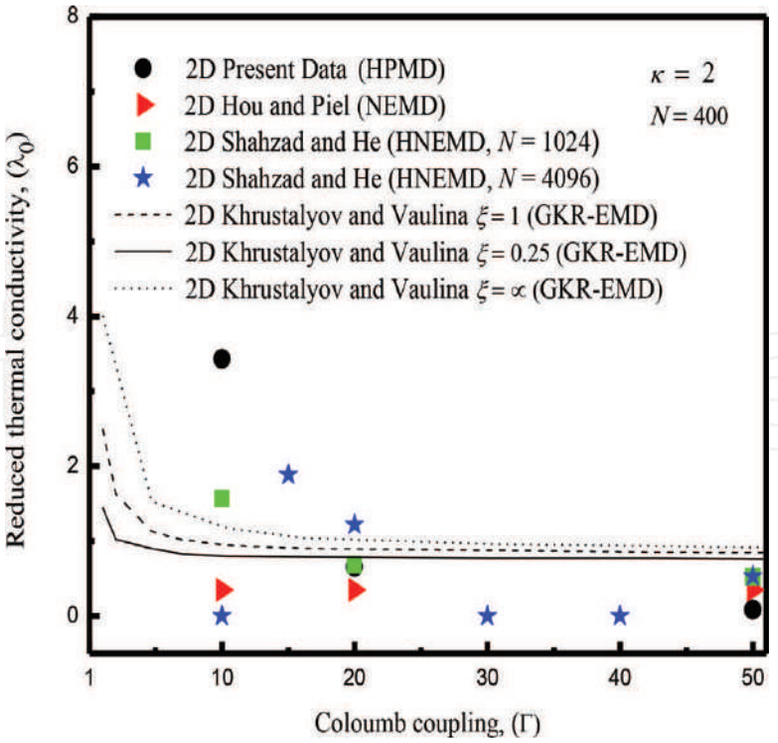

Figure 2. Comparison of results obtained from Yukawa thermal conductivity λ_0 (normalized by ω_p) as a function of plasma coupling Γ ($1 \le \Gamma \le 50$) (system temperature) for SCCDPs at $\kappa = 2$.

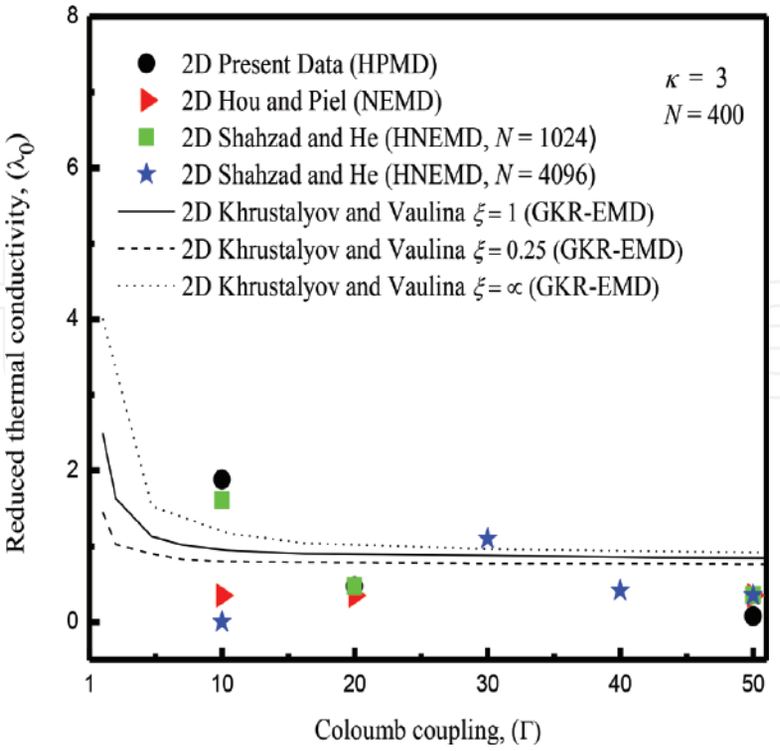

Figure 3. Comparison of results obtained from Yukawa thermal conductivity λ_0 (normalized by ω_p) as a function of plasma coupling Γ ($1 \leq \Gamma \leq 50$) (system temperature) for SCCDPs at $\kappa = 3$.

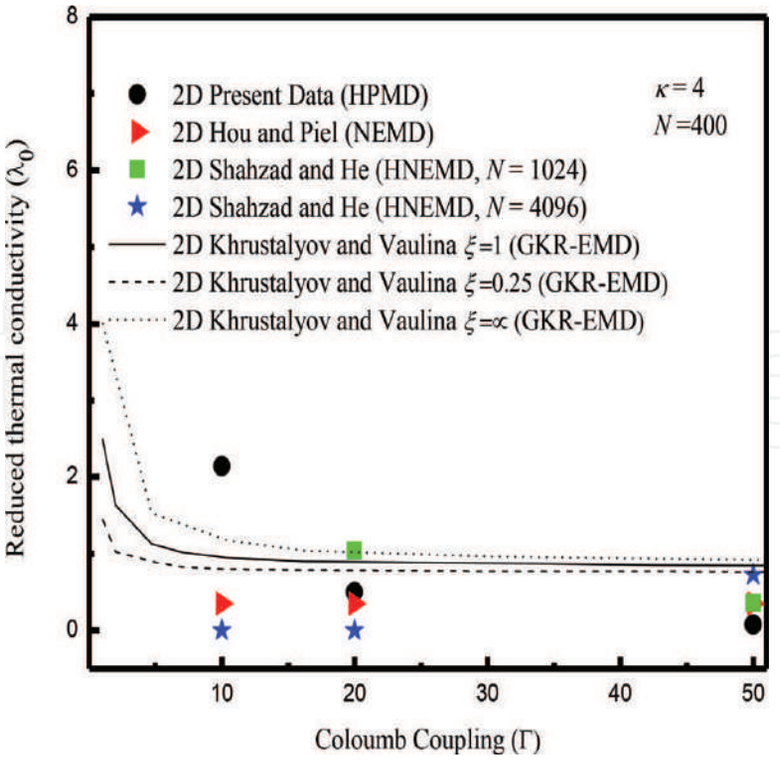

Figure 4. Comparison of results obtained from Yukawa thermal conductivity λ_0 (normalized by ω_p) as a function of plasma coupling Γ ($1 \leq \Gamma \leq 50$) (system temperature) for SCCDPs at $\kappa = 4$.

Figures 1 and **2** show the thermal conductivity for the cases of κ = 1.4 and 2, respectively. For both cases, our simulations cover the appropriate range of Coulomb coupling parameter i.e., from the nearly liquid state to strongly coupled states. It is observed that our investigation of λ_0 at low value of Γ (= 10) is definitely higher than that of GKR-EMD estimations of Khrustalyov and Vaulina [17] and NEMD of Hou and Piel [18] but for κ = 1.4 results are slightly higher than HNMED (N = 1024) simulations of Shahzad and He [19]. It is noted that our result for the low value of Γ shows that particle–particle interactions are very weak and particles have maximum kinetic energy and the effectiveness of screening parameter is large. At intermediate to higher Γ (= 20, 50), the present results lie closer to earlier 2D NEMD simulations [18] and HNMED (N = 4096) computations [19] but slightly less than 2D dissipative Yukawa GKR-EMD numerical results [17]. For both cases, it can be seen that the presented λ_0 is well matched with earlier 2D numerical estimations [19] at intermediate Γ (= 20). It is significant to note that a constant λ_0 is observed at intermediate to higher plasma coupling Γ at constant external perturbation F^* = 0.02; however, it is observed that a very slightly decreasing behavior is observed at higher Γ, contrary to earlier simulations of Shahzad and He [19]. But it is examined that a constant λ_0 is found at intermediate to higher Γ at constant F^*.

Two further set of simulations is plotted to illustrate the plasma λ_0 behaviors of the simulated complex dusty plasmas at a higher value of screening. For this case, **Figures 3** and **4** show the normalized λ_0 computed by the HPMD approach for N = 400 at κ = 3 and 4 and a sequence of different simulations are performed. It is characterized by these figures that the present results lie close to the earlier 2D NEMD results of Hou and Piel [18] at intermediate to higher Γ (= 20, 50). For the κ = 3 at a lower value of Γ, our simulation result is slightly higher than earlier HNMED simulation result, however, for both cases at a lower value of Γ, it is definitely higher than earlier numerical results of NEMD, GKR-EMD.

11. Conclusions

The improved Evan-Gillan HPMD method is used to investigate the thermal conductivity of the 2D strongly coupled complex Yukawa liquid for a suitable range of plasma parameters of screening lengths κ (=1, 4) and Coulomb couplings Γ (=1, 100). Nonequilibrium molecular dynamics method uses the thermal response of heat energy current to calculate the preliminary results of plasma thermal conductivity. The presented method is better than earlier HNEMD and NEMD methods because the very small value of external perturbation (F^* = 0.02) is only imposed on several individual particles each time step. It is concluded that the present approach for evaluating the thermal conductivity from homogenous PMD method yields consistent results and this method is quite accurate and much faster than the previous EMD and NEMD methods. For future work, the system size (N) and external perturbation strength (F^*) can be varied to examine how effectively this improved HPMD algorithm calculates the thermal conductivities of Yukawa and other Coulomb systems. It is suggested that the presented HPMD technique based on Ewald summation described here can be used to explore the ionic and dipolar materials.

Acknowledgements

The authors thank the National Advanced Computing Centre of National Centre for Physics (NCP), Pakistan and National High-Performance Computing Center (NHPCC) of Xian Jiaotong University, P.R. China for allocating computer time to test and run our MD code.

Abbreviations

SCCDPs	strongly coupled complex dusty plasmas
EMD	equilibrium molecular dynamics
HNEMD	homogeneous nonequilibrium molecular dynamics
HPMD	homogeneous perturbed molecular dynamics
MMDS	molecular mechanics dynamic simulation
DPLs	dusty plasma liquids
LRT	linear response theory
GKR	Green-Kubo relation
CDPs	complex dusty plasma
PBCS	periodic boundary conditions
Γ	Coulomb coupling
κ	screening strength
λ_D	Debye length
K_B	Boltzmann constant

Author details

Aamir Shahzad[1,2]*, Syed Irfan Haider[1], Maogang He[2] and Yan Feng[3]

*Address all correspondence to: aamirshahzad_8@hotmail.com

1 Molecular Modeling and Simulation Laboratory, Department of Physics, Government College University Faisalabad (GCUF), Faisalabad, Pakistan

2 Key Laboratory of Thermo-Fluid Science and Engineering, Ministry of Education (MOE), Xi'an Jiaotong University, Xi'an, China

3 Center for Soft Condensed Matter Physics and Interdisciplinary Research, College of Physics, Optoelectronics and Energy, Soochow University, Suzhou, China

References

[1] Shukla PK, Mamun AA. Series in Plasma Physics: Introduction to Dusty Plasma Physics. Bristol: Taylor & Francis group, CRC Press; 2001; ISBN: 9780750306539 – CAT#IP39

[2] Merlino RL. Dusty Plasmas and Applications in Space and Industry. Plasma Physics Applied. 2006; ISBN: 81-7895-230-0

[3] Bellan PM. Fundamentals of Plasma Physics. 1st ed. UK: Cambridge University Press; 2008. ISBN-13: 9780521528009

[4] Shukla PK. Dusty Plasmas: Physics, Chemistry and Technological Impacts in Plasma Processing. In: Bouchoule A. Wiley, New York. 2000; ISBN: 0471973866

[5] Chen FF. Introduction to Plasma Physics and Controlled Fusion. 2nd ed. New York: Springer-Verlag. 2006; 200 p. ISBN: 9780521825689

[6] Thomas H, Morfill GE, Demmel V, Goree J, Feuerbacher B, Möhlmann D. Plasma crystal: Coulomb crystallization in a dusty plasma. Physical Review Letters. 1994;**73**(5):652. DOI: 0031-9007/94

[7] Shahzad A, He M-G. Thermal conductivity calculation of complex (dusty) plasmas. Physics of Plasmas. 2012;**19**(8):083707. DOI: 10.1063/1.4748526

[8] Kikuchi H. Electrohydrodynamics in Dusty and Dirty Plasmas: Gravito-Electrodynamics and EHD. Dordrecht; Boston: Kluwer Academic Publishers; 2001. 207 p. ISBN: 0792368223

[9] Peratt AL. Physics of the Plasma Universe, Appendix C. Dusty and Grain Plasmas. New York: Springer; 1992. ISBN: 0-387-97575-6

[10] Boulos MI, Fauchais P, Pfender E. Thermal Plasmas: Fundamentals and Applications. New York: Springer Science & Business Media; 2013. DOI: 10.1007/978-1-1337-1

[11] Shahzad A, He M-G. Thermal Conductivity and Non-Newtonian Behavior of Complex Plasma Liquids, A Chapter from the Book of Thermoelectrics for Power Generation—A Look at Trends in the Technology. Ri jeka, Croatia: InTech; 2016; 305 p. DOI: 10.5772/65563

[12] Vladimir EF, Gregor EM. Complex and Dusty Plasmas: From Laboratory to Space. Bosa Roca, Uni ted States: Taylor & Francis Inc, CRC Press Inc.; 2010; ISBN-10: 1420083112/ ISBN-13: 9781420083118

[13] Faussurier G, Murillo MS. Gibbs-Bogolyubov inequality and transport properties for strongly coupled Yukawa fluids. Physical Review E. 2003;**67**(4):046404. DOI: 10.1103/ PhysRevE.85.046405

[14] Gillan MJ, Dixon M. The calculation of thermal conductivities by perturbed molecular dynamics simulation. Journal of Physics C: Solid State Physics. 1983;**16**(5):869. DOI: 0022-3719/83/050869

[15] Mazars M. Ewald sums for Yukawa potentials in quasi-two-dimensional systems. The Journal of Chemical Physics. 2007;**126**(5):056101. DOI: 10.1063/1.2431371

[16] Mandadapu KK, Jones RE, Papadopoulos P. A homogeneous nonequilibrium molecular dynamics method for calculating thermal conductivity with a three-body potential. The Journal of Chemical Physics. 2009;**130**(20):204106. DOI: 10.1063/1.3141982

[17] Khrustalyov YV, Vaulina OS. Numerical simulations of thermal conductivity in dissipative two-dimensional Yukawa systems. Physical Review E. 2012;**85**(4):046405. DOI: 10.1103/PhysRevE.85.046405

[18] Hou LJ, Piel A. Heat conduction in 2D strongly coupled dusty plasmas. Journal of Physics A: Mathematical and Theoretical. 2009;**42**(21):214025. DOI: 10.1088/1751-8113

[19] Shahzad A, He MG. Numerical experiment of thermal conductivity in two-dimensional Yukawa liquids. Physics of Plasmas. 2015;**22**(12):123707. DOI: 10.1063/1.4938275

Chapter 2

Thermal Conductivity of Ionic Liquids

Daisuke Tomida

Additional information is available at the end of the chapter

http://dx.doi.org/10.5772/intechopen.76559

Abstract

Ionic liquids (ILs) have attracted great attention as green solvents, heat carriers, and electrolytes. They can be obtained with specific thermophysical properties and functions by changing the kind of species of cations and anions. Knowledge of the fundamental thermophysical properties of ILs, such as their densities, viscosities, and thermal conductivities, is needed to design ILs with desirable thermophysical properties. In this chapter, we will review the various measurement results for the thermal conductivities of the pure components of ILs and methods for predicting the thermal conductivity of an IL, which are based on its structure and physical properties, by conducting correlations between these parameters. In the recent years, the thermal conductivities of IoNano fluids, which comprise of nanoparticles dispersed in an IL, have attracted great attention. Therefore, we will review the unique thermal conductivities of IoNano fluids.

Keywords: thermal conductivity, ILs, nanofluids, correlation, prediction

1. Introduction

ILs are salts that exist in the liquid at ambient temperature, and their characteristics include nonvolatility, flame retardancy, high ionic conductivity, and exhibiting a liquid state at a wide temperature range, among others. Since Wilkes et al. discovered a water-stable IL system using BF_4^-, a nonchloroaluminate anion, in 1992 [1], the study of ILs has drastically increased, and ILs have drawn great attention for a variety of applications, such as an alternative reaction solvent to replace organic solvents, as thermal medium, and as electrolyte in batteries. **Figure 1** shows the cations and anions that are typically used in ILs. There are infinite potential combinations of cations and anions and, additionally, various chemical modifications can be made to the organic moieties of the ions. Thus, there is a possibility of creating ILs tailored for specific purposes; for this reason, ILs are also called "designer solvents."

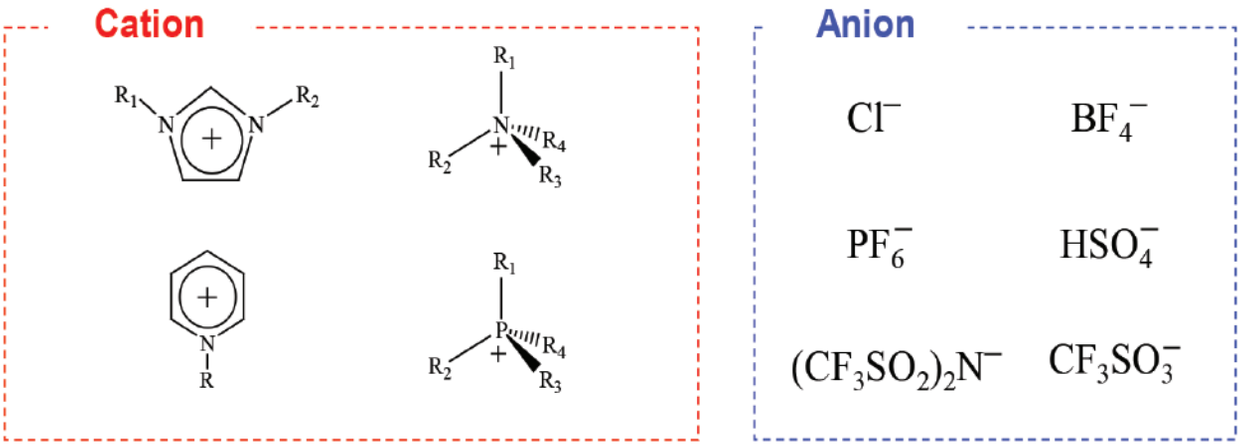

Figure 1. Cations and anions typically used in ILs.

A variety of ILs have been synthesized, many of which have melting points much greater than room temperature. For this reason, ILs are broadly defined as the ones having melting point below 100°C. Numerous ILs have been created; however, the prediction of their thermophysical properties such as the thermal conductivity on the basis of the molecular structure would be useful to develop novel ILs. In this chapter, we review the various measurement results for the thermal conductivities of the pure components of IL, the progress made toward the development of effective methods of correlating and predicting the thermal conductivities, and the thermal conductivities of IoNano fluids, which, in the recent years, have attracted great attention as high-temperature heat mediums.

2. Thermal conductivities of the pure components of ILs

2.1. Investigating the thermal conductivities of ILs

The thermal conductivity of an IL was first reported by Valkenburg et al. [2]. The known thermophysical properties of ILs, including their thermal conductivities, are summarized in ILs database of NIST [3]. During the early stages of IL research, since it was necessary to synthesize an IL to measure its thermophysical properties, there was less number of researches. However, once ILs became commercially available, the amount of information reported about the thermophysical properties of ILs increased drastically. However, the number of the reported thermal conductivity values is fewer than the other thermophysical properties, and it has been reported that two or three component systems have almost no thermal conductivity. Only four research groups have reported the thermal conductivities of binary mixtures [4–7], and only two groups have reported on ternary mixtures containing ILs [6, 8]. The reported thermal conductivity values for various ILs range from 0.106 [4] to 0.238 W/(m K) [7] at 298.15 K (**Figure 2**) and many reported values are around 0.15 W/(m K) [3, 9] (**Figure 3**). The thermal conductivities of ILs were found to be about the same as those of organic solvents, such as methanol and toluene.

http://dx.doi.org/10.5772/intechopen.76559

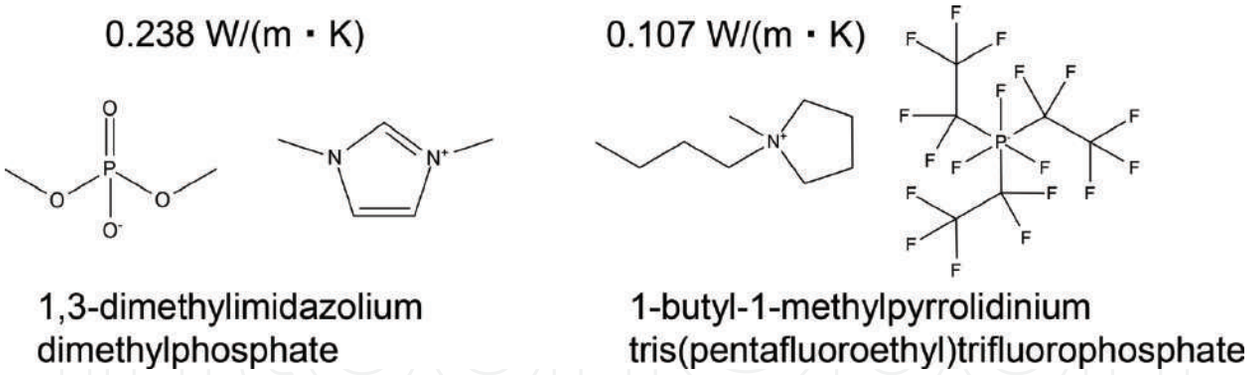

Figure 2. The ILs with the highest thermal conductivity (left) [7] and the lowest thermal conductivity (right) [4] at 298.15 K that have been reported to date.

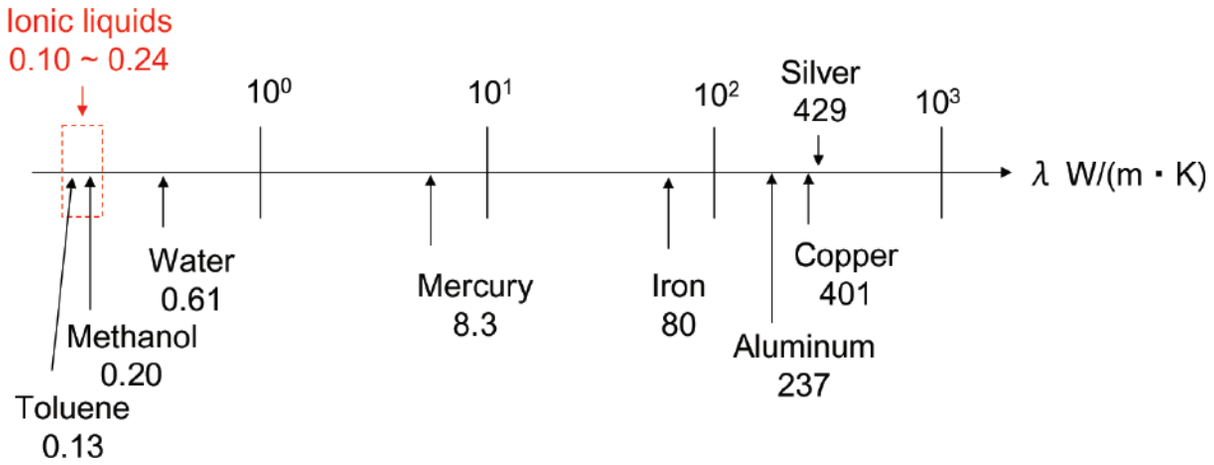

Figure 3. Thermal conductivities of various substances at 298.15 K [3, 9].

It is well known that the thermophysical properties of ILs are influenced by impurities [10]. For example, it has been reported that the viscosity of an IL decreases by about 1% with the addition of only 100 ppm of water [11]. The influence of trace water and chloride on the thermal conductivity of an IL has been reported to be relatively small compared to that on the other thermophysical properties, such as viscosity and density, as reported by Rooney et al. [4] (**Figure 4**). Our group has also investigated the effect of chloride ions on the thermal conductivities of IL [5] by measuring and comparing the thermal conductivity of 1-butyl-3-methylimidazolium tetrafluoroborate with different chloride concentrations of 421 and 4580 ppm; the difference between the thermal conductivities of these ILs was 1.2%.

We additionally investigated the influence of the alkyl chain length on thermal conductivity of ILs [12–16]. **Figure 5** shows the relation between alkyl chain length and thermal conductivity at 293 K. The thermal conductivity of *n*-alkanes was calculated by REFPROP 9.0 [17]. The results indicated that the alkyl chain length does not significantly affect the thermal conductivity. This observation differed from the findings of other studies regarding the thermal conductivities of *n*-alkanes [18] and the influence of the viscosity of the IL [19].

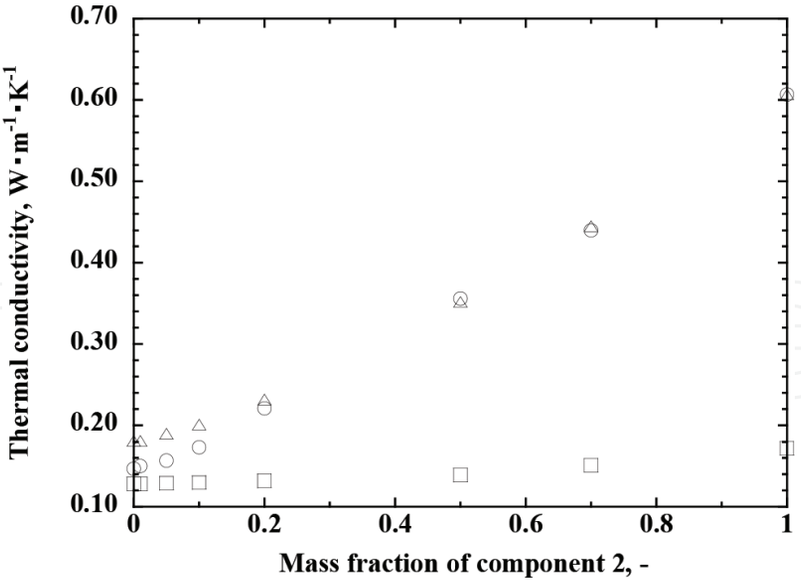

Figure 4. Effects of water and chloride on the thermal conductivities of ILs [4]: °, 1-butyl-3-methylimidazolium trifluoromethanesulfonate (1) + water (2); Δ, 1-ethyl-3-methylimidazolium ethylsulfate (1) + water (2); □, 1-hexyl-3-methylimidazolium bis-(trifluoromethylsulfonyl)imides (1) + 1-hexyl3-methylimidazolium chloride (2).

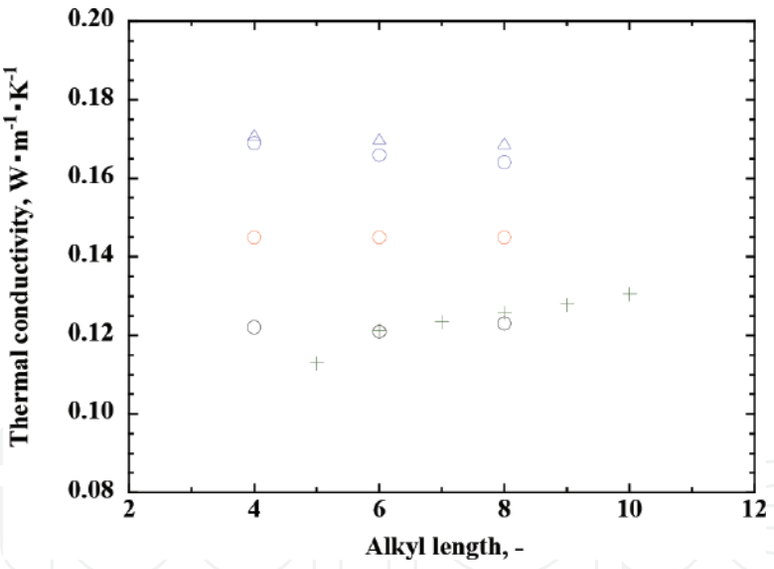

Figure 5. Relationship between the alkyl chain length and the thermal conductivities of various ILs at 293 K: 1-alkyl-3-methylimidazolium hexafluorophosphates; 1-alkyl-3-methylimidazolium tetrafluoroborates; 1-alkyl-3-methylimidazolium bis[(trifluoromethyl)sulfonyl] amides; *N*-alkylpyridinium tetrafluoroborates; and *n*-alkanes [12–17].

The temperature and pressure dependence of the thermal conductivity of ILs has been investigated [12, 14]. **Figure 6** shows a comparison of the temperature dependence of thermal conductivities of various ILs and organic solvents. The results showed that the temperature dependence of the thermal conductivity of each IL is very small in comparison with those of toluene and benzene. This is because the temperature dependence of the density of an IL is small. **Figure 7** shows a comparison of the thermal conductivities of various ILs and organic

http://dx.doi.org/10.5772/intechopen.76559

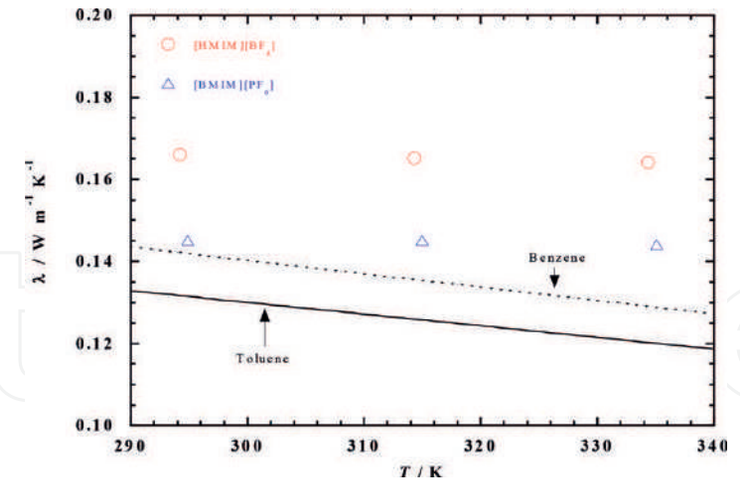

Figure 6. Temperature dependences of the thermal conductivities of various ILs and organic solvents.

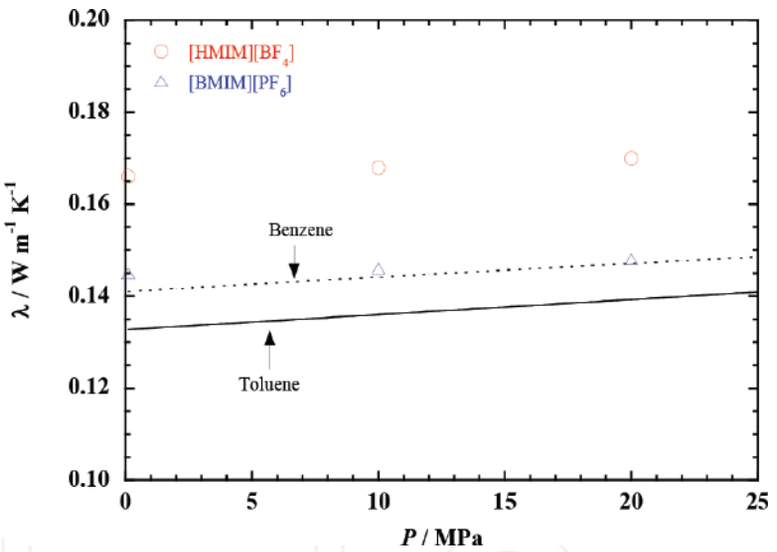

Figure 7. Pressure dependences of the thermal conductivities of various ILs and organic solvents.

solvents as functions of the pressure. It was found that the pressure dependence of the thermal conductivity of each IL is very small (within 20 MPa) in comparison with those of toluene and benzene. This is because the pressure dependence of the density of an IL is small.

2.2. Prediction and correlation of the thermal conductivity of an IL with its physical properties

A variety of ILs has been created as "designer solvents." Therefore, the prediction of the thermal conductivity of an IL based on its structure and other physical properties would be very useful for designing novel ILs. So far, an empirical-prediction method [13, 20, 21], group-contribution method [22–24], quantitative structure-property relationship method [25], prediction

method using a neural network [26, 27], and many other methods [28–35] have been proposed for the prediction of the thermal conductivities of ILs. In this section, the empirical-prediction method based on other physical properties and prediction method using group-contribution method are introduced.

We proposed a correlation equation based on the Mohanty equation [36] to describe the relation between the thermal conductivity and viscosity of an IL [13]:

$$\log\left(M\lambda/\eta\right) = 1.9596 - 0.004499\ M, \tag{1}$$

where M is the molar mass, λ is the thermal conductivity, and η is the viscosity of the IL. However, Eq. (1) was obtained by assuming that the molar mass of the IL is two times larger than the actual value. Fröba et al. proposed another correlation method and described the relation between the thermal conductivity and density of an IL as follows [20]:

$$\lambda M\rho = 0.1244M + 18.84\ , \tag{2}$$

where M is the molar mass, λ is the thermal conductivity, and ρ is the density of the IL. From 45 data points for 36 ILs, the standard deviation and mean absolute deviation of the experimental data relative to the predictions were 7.8 and 6.5%, respectively at 293.15 K and atmospheric pressure. Koller et al. extended this model to calculate the thermal conductivity at any temperature as follows [21]:

$$\lambda(T) = \left(0.0960 + \frac{21.43}{M\rho(T_{\mathrm{ref}})}\right)\left(\frac{\rho(T)}{\rho(T_{\mathrm{ref}})}\right)^{0.826} \tag{3}$$

From 469 data points for 53 different ILs, the mean absolute deviation and root-mean-square deviation of the experimental data relative to the values predicted using Eq. (3) were 4.81 and 6.32%, respectively.

As mentioned above, novel ILs are synthesized and many new substances will be synthesized in the near future. Therefore, it would be very useful to predict the thermophysical properties from the structure of an IL.

Gardas and Coutinho proposed predicting the thermal conductivity of an IL by the group-contribution method [22]. When this method was proposed, few reports were available regarding the thermal conductivities of ILs from which a prediction equation could be derived. However, the following equation was derived to correlate the thermal conductivity to the specific cation and anion and the length of the alkyl chain of the cation:

$$\lambda = A_\lambda - B_\lambda T\ , \tag{4}$$

where T is the temperature in K and A_λ and B_λ are the fitting parameters that can be obtained from the group-contribution approach. These parameters can be derived as follows:

$$A_\lambda = \sum_{i=1}^{k} n_i a_{i,\lambda} \qquad B_\lambda = \sum_{i=1}^{k} n_i b_{i,\lambda}\,, \tag{5}$$

where n_i is the number of groups of type i, k is the total number of different groups in the molecule, and the parameters $a_{i,\lambda}$, and $b_{i,\lambda}$ estimated for the ILs studied are given in **Table 1**.

Wu et al. proposed a prediction formula in which the group is divided finely so that more ILs can be predicted based on their structures [24]:

$$\lambda = \sum_{i=0}^{2} a_i \left(\sum_{j=1}^{k} n_j \Delta\lambda_{0,j} \right)^i \left[1 + k_0 (1 - T_r)^{2/3}\right]\,, \tag{6}$$

where $T_r = T/T_c$ is the reduced temperature, T_c is the critical temperature in K (which is easy to obtain for many ILs by applying the group-contribution method proposed by Valderrama group [37]), k_0 is the temperature-independent constant, n_j is the number of groups of type j, k is the total number of different groups in the molecule, and the parameters a_i and $\Delta\lambda_{0,j}$ are estimated using **Table 2**. The calculated values and those reported in the literature were in agreement for 286 data points for 36 ILs with an average absolute deviation of 1.66%.

Species	$a_{i,\lambda}$	$b_{i,\lambda}$ **(K^{-1})**
Cations		
1,3-dimethylimidazolium (+)	0.1356	1.564×10^{-5}
1,1-dimethylpyrrolidinium (+)	0.1325	1.668×10^{-5}
Tetramethylphosphonium (+)	0.1503	3.230×10^{-5}
Anions		
PF_6^-	0.0173	9.088×10^{-6}
BF_4^-	0.0874	8.828×10^{-5}
Tf_2N^-	0.0039	2.325×10^{-5}
$CF_3SO_3^-$	0.0305	5.284×10^{-5}
$EtSO_4^-$	0.0700	6.552×10^{-5}
Cl^-	0.0166	1.000×10^{-5}
Groups		
CH_2	0.0010	2.586×10^{-6}
CH_3	0.0042	7.768×10^{-6}

Table 1. Group-contribution parameters, $a_{i,j}$ and $b_{i,j}$, for Eq. (5) at 293–390 K [22].

Without rings		With rings		Coefficients	Values
Group	Values of $\Delta\lambda_{0,j}$	Group	Values of $\Delta\lambda_{0,j}$		
$-CH_3$	−2.66388	>C=	−0.90423	k_0	4.05711
$-CH_2-$ (*with ammonium-*)	0.60575	=CH–	−1.32204	a_0	0.03647
$-CH_2-$ (*with phosphonium-*)	0.71023	$-CH_2-$	−0.49677	a_1	−0.00097
$-CH_2-$ (*with others*)	0.68295	>CH–	2.20488	a_2	0.00003
>C<	−0.36265	–NH–	2.53635		
>CH	5.29795	–N=	0.83850		
–CN	1.51636	>N–/>N<$^+$	−3.22547		
–COO–	1.51468				
–COOH	−10.35869				
>N–/>N<$^+$/–N–$^-$	−1.24392				

Without rings	
Group	Values of $\Delta\lambda_{0,j}$
$-NH_2$	−3.20298
$-SO_2$	6.88560
–O–/[–O]$^-$	0.00273
–OH	−1.33002
–F	1.69009
–Cl	−6.92175
–B	−3.97751
–P	−2.50897

Table 2. The coefficient values obtained by the group-contribution method using Eq. (6) [24].

Lazzús proposed a prediction equation to calculate the thermal conductivity of an IL as a function of the temperature and pressure [23]. The experimentally measured thermal conductivities of 41 ILs (including 400 experimental data points) in the range of 0.1–0.22 W/(m K) were used to design the proposed method for the temperature range of 273–390 K and the pressure range of 0.1–20 MPa. The results showed that the proposed group-contribution method can be used to accurately predict the thermal conductivity of an IL as a function of the temperature and pressure present with lower deviations between the predicted and actual values, including an average absolute relative deviation (AARD) of less than 1.90% and an R^2 of 0.9879 for the correlation dataset and AARD of less than 2.33% and R^2 of 0.9754 for the prediction dataset.

3. Thermal conductivities of IoNano fluids

Nanofluids are dispersions of nanoparticles and are expected to be applied as heat transfer media and used for inkjet printing. They were first reported by Choi [38] in 1995. Since then, it has been reported that the thermal conductivity of ethylene glycol is improved by 40% when 0.3 vol% of 10-nm Cu nanoparticles are dispersed in ethylene glycol [39]. A dispersion of nanoparticles in an IL is called an "IoNano fluid," as first dubbed by Castro et al. in 2010 in a

study of the thermal conductivities of nanofluids with carbon nanotubes dispersed in ILs [40, 41]. As described above, the thermal conductivities of ILs have been reported to be about the same as those of ethanol and methanol, which is not high. For this reason, it is expected that the thermal conductivity of an IL can be enhanced by dispersing nanoparticles in it.

It is known that the thermal conductivity of a nanofluid agrees well with the Hamilton-Crosser model [42]:

$$\frac{k_{eff}}{k_0} = \frac{k_p + (n-1)k_0 + (n-1)(k_p - k_0)\phi_p}{k_p + (n-1)k_0 - (k_p - k_0)\phi_p} \tag{7}$$

where k_0, k_{eff}, and k_p are the thermal conductivities of the dispersion medium, nanofluid, and dispersoid, respectively, in W/(m K), n is the particle shape parameter [–], and φ_p is the volume fraction of the dispersoid (also unitless).

Figure 8 shows the calculated enhancement of the thermal conductivity rate based on the Hamilton-Crosser model when silver, alumina, and barium titanate spherical nanoparticles are used as the dispersoid in 1-butyl-3-methylimidazolium tetrafluoroborate ([BMIM][BF_4]) as a representative IL. **Table 3** shows the thermal conductivity of each dispersoid tested. The results show that even with dispersoids with significantly different thermal conductivities, the resulting enhancement in the thermal conductivity does not vary significantly when the volume fraction is about 15% (n = 3). This suggests that, for the case of dispersing spherical nanoparticles in an IL, the thermal conductivity of the dispersoid does not significantly affect the thermal conductivity of the obtained nanofluid. Thus, to further increase the thermal conductivity of an IL using spherical nanoparticles, the volume fraction of the dispersoid must be increased; however, this introduces a problem of flowability. Therefore, while considering the use of a nanofluid as a heating medium, it is necessary to increase the thermal conductivity using the smallest possible volume fraction of nanoparticles. To remarkably increase the thermal conductivity enhancement rate with a low nanoparticle concentration, it is necessary

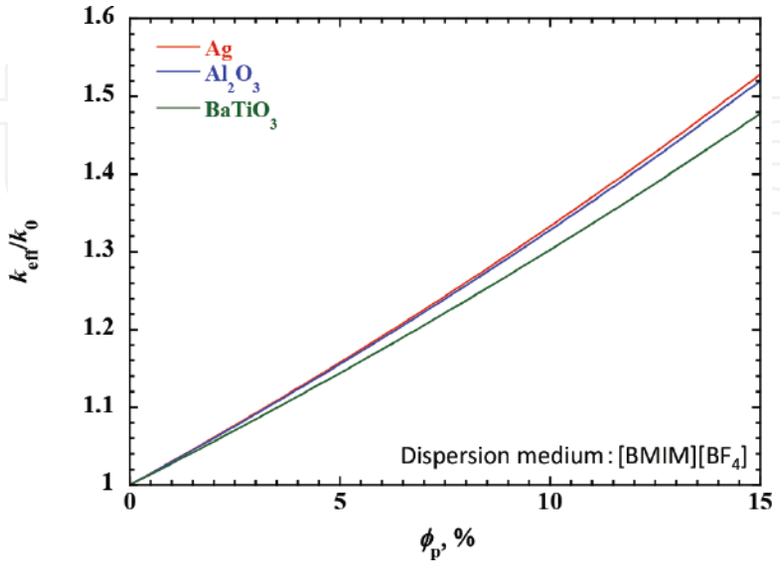

Figure 8. Relationship between the enhancement of the thermal conductivity and the volume fraction of nanoparticles based on the Hamilton-Crosser model at 298 K.

	k_p, W/(m K)
Ag	428
Al_2O_3	36
$BaTiO_3$	6

Table 3. Thermal conductivities of dispersoids.

to increase the particle diameter, *n*. Increasing *n* increases the slope; this is possible by using a material with a large aspect ratio.

Wang et al. reported that the thermal conductivity of an IoNano fluid of carbon nanotubes dispersed in 1-hexyl-3-methylimidazolium tetrafluoroborate (**Figure 9**) [43] was improved by more than 10% by adding only 0.03 wt% of graphene. In addition, the results showed that the thermal conductivities of the pure IL component (the dispersion medium) and the IoNano fluid increase with an increase in temperature. **Figure 6** shows the temperature dependence of the thermal conductivities of benzene, toluene, and 1-hexyl-3-methylimidazolium tetrafluoroborate. Usually, the thermal conductivity of a liquid decreases with increasing temperature; it is known that this holds true for ILs and that the temperature dependence of an IL is smaller than those of organic solvents including benzene and toluene. The thermal conductivity values of [HMIM][BF_4] reported by other researchers [40] indicate that the thermal conductivity gradually decreases as the temperature increases. Thus, it is conceivable that the thermal conductivity value reported by Wang et al. was influenced by convection. Assael et al. studied the reported thermal conductivity values of the nanofluid in detail and pointed out that there are many reported cases that are affected by convection [44, 45]. Based on this finding, it is necessary to carefully consider the previously reported thermal conductivity values for nanofluids because they may include the influence of convection.

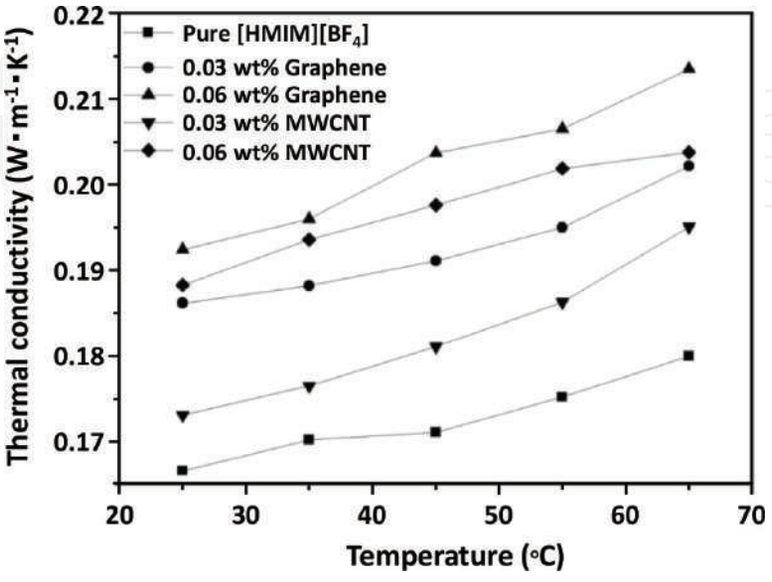

Figure 9. Thermal conductivities of IoNano fluids and [HMIM][BF_4] as functions of temperature [43].

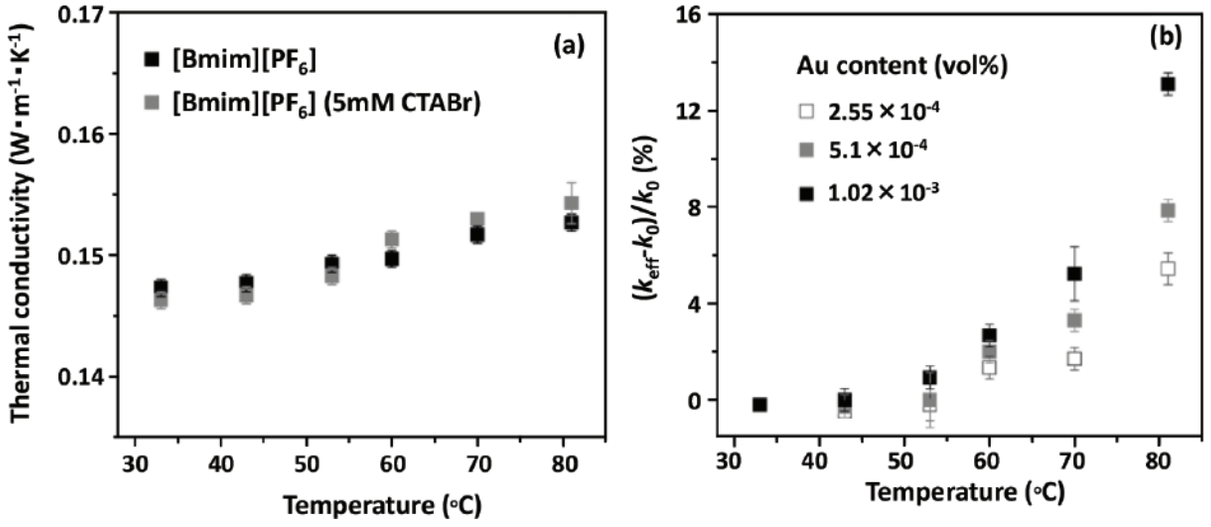

Figure 10. Thermal conductivity of [BMIM][PF_6] over a range of temperatures (a) with and without 5 mmol CTABr and (b) the thermal conductivity enhancement in Au/[BMIM][PF_6] nanofluids due to various Au concentrations [46].

Wang et al. measured the thermal conductivity of Au/[BMIM][PF_6] nanofluids of Au nanoparticles dispersed in a typical IL 1-butyl-3-methylimidazolium hexafluorophosphate medium ([BMIM][PF_6]) [46]. The thermal conductivities of the Au/[Bmim][PF_6] nanofluids stabilized by cetyltrimethylammonium bromide (CTABr) increases with an increase in the temperature and the rate of the increase also increases with an increase in the temperature (**Figure 10**). However, it was also seen that the thermal conductivity of [BMIM][PF_6] increases with an increase in the temperature (**Figure 10(a)**). In the thermal conductivity values of [BMIM][PF_6] reported by other researchers [13, 40], the thermal conductivity gradually decreases as the temperature increases; thus, the thermal conductivity measured by Wang et al. likely contains the influence of convection.

Adriana et al. reported the thermal conductivities of IoNano fluids, such as Al_2O_3/[C_4 mpyrr][NTf_2] and MWCNT/[C_4 mim][$(CF_3SO_2)_2N$]. The results showed that the enhancement rate of the thermal conductivity is almost the same as that predicted based on the Hamilton-Crosser equation; no significant enhancement in thermal conductivity has been confirmed in these systems [47].

França et al. reported that the thermal conductivity improved from 4 to 26% between MWCNT/[C_4mim][$CF_3SO_2]_2N$] and MWCNT/[C_2mim][$EtSO_4$] [48]. Although the measurements were obtained by commercial equipment, KD2 Pro, which introduces a large measurement uncertainty, the thermal conductivity was found to gradually decrease with an increase in the temperature in the pure IL component and IoNano fluid; this indicates that the measured values were almost not affected by convection.

4. Summary

In this study, the thermal conductivities of ILs and IoNano fluids were reviewed. The thermal conductivity is one of the physical properties of ILs for which few studies have been reported. The thermal conductivity of an IL is difficult to measure and the observed data are often

influenced by convection. Although the prediction and the correlation method have been proposed and examined, the results are not useful unless they are based on precisely measured values. Therefore, it is necessary to precisely measure and publish more data regarding the thermal conductivities of ILs and IoNano fluids.

Author details

Daisuke Tomida

Address all correspondence to: daisuke.tomida.e4@tohoku.ac.jp

Institute of Multidisciplinary Research for Advanced Materials, Tohoku University, Sendai, Japan

References

[1] Wilkes JS, Zaworotko MJ. Air and water stable 1-ethyl-3-methylimidazolium based ionic liquids. Journal of the Chemical Society, Chemical Communications. 1992;965-967

[2] Valkenburg MEV, Vaughn RL, Williams M, Wilkes JS. Thermochemistry of ionic liquid heat-transfer fluids. Thermochimica Acta. 2005;**425**:181-188

[3] Ionic Liquids Database—ILThermo (National Institute of Standards and Technology, 2006). http://ILThermo.boulder.nist.gov/ILThermo/ [Accessed: January 2018]

[4] Ge R, Hardacre C, Nancarrow P, Rooney DW. Thermal conductivities of ionic liquids over the temperature range from 293 K to 353 K. Journal of Chemical & Engineering Data. 2007;**52**:1819-1823

[5] Tomida D, Kenmochi S, Tsukada T, Qiao K, Yokoyama C. Thermal conductivities of imidazolium-based ionic liquid + CO_2 mixtures. International Journal of Thermophysics. 2010;**31**:1888-1895

[6] Chen Q-L, Wu K-J, He C-H. Thermal conductivities of [EMIM][$EtSO_4$], [EMIM][$EtSO_4$] + C_2H_5OH, [EMIM][$EtSO_4$] + H_2O, and [EMIM][$EtSO_4$] + C_2H_5OH + H_2O at T = (283.15 to 343.15) K. Journal of Chemical and Engineering Data. 2013;**58**:2058-2064

[7] Chen W, Qiu L, Liang S, Zheng X, Tang D. Measurement of thermal conductivities of [mmim]DMP/CH_3OH and [mmim]DMP/H_2O by freestanding sensor-based 3ω technique. Thermochimica Acta. 2013;**560**:1-6

[8] Yusoff R, Shamiri A, Aroua MK, Ahmady A, Shafeeyan MS, Lee WS, Lim SL, Burhanuddin SNM. Physical properties of aqueous mixtures of N-methyldiethanolamine (MDEA) and ionic liquids. Journal of Industrial and Engineering Chemistry. 2014;**20**:3349-3355

[9] Japan Society of Thermophysical Properties. Thermophysical Properties Handbook. Tokyo: Yokendo; 2008

[10] Seddon KR, Stark A, Torres MJ. Influence of chloride, water, and organic solvents on the thermophysical properties of ionic liquids. Pure and Applied Chemistry. 2000;**72**: 2275-2287

[11] Widegren JA, Laesecke A, Magee JW. The effect of dissolved water on the viscosities of hydrophobic room-temperature ionic liquids. Chemical Communications. 2005; 1610-1612

[12] Tomida D, Kenmochi S, Tsukada T, Yokoyama C. Measurements of thermal conductivity of 1-butyl-3-methylimidazolium tetrafluoroborate at high pressure. Heat Transfer—Asian Research. 2007;**36**:361-372

[13] Tomida D, Kenmochi S, Tsukada T, Qiao K, Yokoyama C. Thermal conductivities of [bmim][PF_6], [hmim][PF_6], and [omim][PF_6] from 294 to 335 K at pressures up to 20 MPa. International Journal of Thermophysics. 2007;**28**:1147-1160

[14] Tomida D, Kenmochi S, Tsukada T, Qiao K, Bao Q, Yokoyama C. Viscosity and thermal conductivity of 1-hexyl-3-methylimidazolium tetrafluoroborate and 1-octyl-3-methylimidazolium tetrafluoroborate at pressures up to 20 MPa. International Journal of Thermophysics. 2012;**33**:959-969

[15] Tomida D, Kenmochi S, Qiao K, Tsukada T, Yokoyama C. Densities and thermal conductivities of *N*-alkylpyridinium tetrafluoroborates at high pressure. Fluid Phase Equilibria. 2013;**340**:31-36

[16] Tomida D, Kanno S, Qiao K, Yokoyama C. Viscosities at pressures up to 20 MPa and thermal conductivities at 0.1 MPa of 1-alkyl-3-methylimidazolium bis[(trifluoromethyl) sulfonyl]amides. High Temperatures—High Pressures. 2017;**46**:231-245

[17] Lemmon EW, Huber ML, McLinden MO. NIST Standard Reference Data 23. REFPROP Version 9.1. CO: NIST; 2013

[18] Watanabe H, Seong DJ. The thermal conductivity and thermal diffusivity of liquid *n*-alkanes: C_nH_{2n+2} (n=5 to 10) and toluene. International Journal of Thermophysics. 2002;**23**:337-356

[19] Seddon KR, Stark A, Torres MJ. Viscosity and density of 1-alkyl-3-methylimidazolium ionic liquids. ACS Symposium Series. 2002;**819**:34-49

[20] Fröba AP, Rausch MH, Krzeminski K, Assenbaum D, Wasserscheid P, Leipertz A. Thermal conductivity of ionic liquids: Measurement and prediction. International Journal of Thermophysics. 2010;**31**:2059-2077

[21] Koller TM, Schmid SR, Sachnov SJ, Rausch MH, Wasserscheid P, Fröba AP. Measurement and prediction of the thermal conductivity of tricyanomethanide- and tetracyanoborate-based imidazolium ionic liquids. International Journal of Thermophysics. 2014;**35**:195-217

[22] Gardas RL, Coutinho JAP. Group contribution methods for the prediction of thermophysical and transport properties of ionic liquids. AICHE Journal. 2009;**55**:1274-1290

[23] Lazzus JA. A group contribution method to predict the thermal conductivity λ(T,P) of ionic liquids. Fluid Phase Equilibria. 2015;**405**:141-149

[24] Wu KJ, Zhao CX, He CH. Development of a group contribution method for determination of thermal conductivity of ionic liquids. Fluid Phase Equilibria. 2016;**339**:10-14

[25] Lazzús JA, Pulgar-Villarroel G. Estimation of thermal conductivity of ionic liquids using quantitative structure-property relationship calculations. Journal of Molecular Liquids. 2015;**211**:981-985

[26] Hezave AZ, Raeissi S, Lashkarbolooki M. Estimation of thermal conductivity of ionic liquids using a perceptron neural network. Industrial and Engineering Chemistry Research. 2012;**51**:9886-9893

[27] Lazzús JA. Estimation of the thermal conductivity $\lambda(T,P)$ of ionic liquids using a neural network optimized with genetic algorithms. Comptes Rendus Chimie. 2016;**19**:333-341

[28] Carrete J, Méndez-Morales T, García M, Vila J, Cabeza O, Gallego LJ, Varela LM. Thermal conductivity of ionic liquids: A pseudolattice approach. Journal of Physical Chemistry C. 2012;**116**:1265-1273

[29] Shojaee SA, Farzam S, Hezave AZ, Lashkarbolooki M, Ayatollahi S. A new correlation for estimating thermal conductivity of pure ionic liquids. Fluid Phase Equilibria. 2013;**354**:199-206

[30] Chen QL, Wu KJ, He CH. Thermal conductivity of ionic liquids at atmospheric pressure: Database, analysis, and prediction using a topological index method. Industrial and Engineering Chemistry Research. 2014;**53**:7224-7232

[31] Wu KJ, Chen QL, He CH. Speed of sound of ionic liquids: Database, estimation, and its application for thermal conductivity prediction. AICHE Journal. 2014;**60**:1120-1131

[32] Albert J, Müller K. Thermal conductivity of ionic liquids: An estimation approach. Chemical Engineering Science. 2014;**119**:109-113

[33] Atashrouz S, Mozaffarian M, Pazuki G. Modeling the thermal conductivity of ionic liquids and ionanofluids based on a group method of data handling and modified Maxwell model. Industrial and Engineering Chemistry Research. 2015;**54**:8600-8610

[34] Haghbakhsh R, Raeissi S. A novel correlative approach for ionic liquid thermal conductivities. Journal of Molecular Liquids. 2017;**236**:214-219

[35] Oster K, Jacquemin J, Hardacre C, Ribeiro APC, Elsinawi A. Further development of the predictive models for physical properties of pure ionic liquids: Thermal conductivity and heat capacity. The Journal of Chemical Thermodynamics. 2018;**118**:1-15

[36] Mohanty SR. A relationship between heat conductivity and viscosity of liquids. Nature. 1951;**168**:42

[37] Valderrama JO, Forero LA, Rojas RE. Critical properties and normal boiling temperature of ionic liquids. Update and a new consistency test. Industrial and Engineering Chemistry Research. 2012;**51**:7838-7844

[38] Choi SUS. Enhancing thermal conductivity of fluids with nanoparticles. ASME Fluids Engineering Division. 1995;**231**:99-105

[39] Eastman JA, Choi SUS, Li S, Yu W, Thompson LJ. Anomalously increased effective thermal conductivities of ethylene glycol-based nanofluids containing copper nanoparticles. Applied Physics Letters. 2001;**78**:718-720

[40] Nieto de Castro CA, Lourenco MJV, Ribeiro APC, Langa E, Vieira SIC. Thermal conductivity of [$C_{4\ m}$im][$(CF_3SO_2)_2$N] and [$C_{2\ m}$im][$EtSO_4$] and their IoNanofluids with carbon nanotubes: Experiment and theory. Journal of Chemical & Engineering Data. 2010; **55**:653-661

[41] Nieto de Castro CA, Murshed SMS, Lourenço MJV, Santos FJV, Lopes MLM, França JMP. Enhanced thermal conductivity and specific heat capacity of carbon nanotubes ionanofluids. International Journal of Thermal Sciences. 2012;**62**:34-39

[42] Hamilton R, Crosser OK. Thermal conductivity of heterogeneous two-component systems. Industrial and Engineering Chemistry Fundamentals. 1962;**1**:187-191

[43] Wang F, Han L, Zhang Z, Fang X, Shi J, Ma W. Surfactant-free ionic liquid-based nanofluids with remarkable thermal conductivity enhancement at very low loading of graphene. Nanoscale Research Letters. 2012;**7**:314

[44] Tertsinidou G, Assael MJ, Wakeham WA. The apparent thermal conductivity of liquids containing solid particles of nanometer dimensions: A critique. International Journal of Thermophysics. 2015;**36**:1367-1395

[45] Antoniadis KD, Tertsinidou GJ, Assael MJ, Wakeham WA. Necessary conditions for accurate, transient hot-wire measurements of the apparent thermal conductivity of nanofluids are seldom satisfied. International Journal of Thermophysics. 2015;**37**:78

[46] Wang B, Wang X, Lou W, Hao J. Gold-ionic liquid nanofluids with preferably tribological properties and thermal conductivity. Nanoscale Research Letters. 2011;**6**:259

[47] Adriana MA, Georgiana MM, Oana D. Thermal conductivity enhancement by adding nanoparticles to ionic liquids. Solid State Phenomena. 2017;**261**:121-126

[48] França JMP, Vieira SIC, Lourenço MJV, Murshed SMS, Nieto de Castro CA. Thermal conductivity of [$C_{4\ m}$im][$(CF_3SO_2)_2$N] and [$C_{2\ m}$im][$EtSO_4$] and their IoNanofluids with carbon nanotubes: Experiment and theory. Journal of Chemical & Engineering Data. 2013;**58**:467-476

IntechOpen

Chapter 3

Thermal Conductivity in the Boundary Layer of Non-Newtonian Fluid with Particle Suspension

Rudraswamy N.G., Ganeshkumar K.,
Krishnamurthy M.R., Gireesha B.J. and Venkatesh P.

Additional information is available at the end of the chapter

http://dx.doi.org/10.5772/intechopen.76345

Abstract

The present chapter is focused on studies concerned with three-dimensional flow and heat transfer analysis of Carreau fluid with nanoparticle suspension. The heat transfer analysis in the boundary was carried out with the fluid flow over a stretching surface under the influence of nonlinear thermal radiation, mixed convection and convective boundary condition. Suitable similarity transformations are employed to reduce the governing partial differential equations into coupled nonlinear ordinary differential equations. The equations in non-linear form are then solved numerically using Runge-Kutta-Fehlberg fourth fifth-order method with the help of symbolic algebraic software MAPLE. The results so extracted are well tabulated and adequate discussions on the parameters affecting flow and heat transfer analysis were carried out with the help of plotted graphs.

Keywords: Carreau nano fluid, nonlinear thermal radiation, mixed convection, stretching sheet, convective boundary condition, numerical method

1. Introduction

Thermal radiation, the fundamental mechanism of heat transfer is an indispensable activity in rocket propulsion, plume dynamics, solar collector performance, materials processing, combustion systems, fire propagation and other industrial and technological processes at high temperatures. With the developments in computational dynamics, increasing attention has been diverted towards thermal convection flows with the significant radiative flux. Rayleigh initiated the theory of thermal convection, by deriving critical temperature gradient (Critical Rayleigh number). Importance of such radiations is intensified with absolute temperatures at

higher level. Thus a substantial interest is driven towards thermal boundary layer flows with a strong radiation. Governing equation of radiative heat transfer with its integro-differential nature makes numerical solutions of coupled radiative-convective flows even more challenging. Multiple studies were conducted employing several models to investigate heat and mass transfer in boundary layer and fully-developed laminar convection flows. As a consequence several simultaneous multi-physical effects in addition to radiative heat transfer including gravity and pressure gradient effects [1], mhd flow of nanofluids [2], buoyancy effects [3, 4], ferrofluid dynamics [5], stretching surface flow [6, 7], time-dependent, wall injection and Soret/Dufour effects [8–11].

These studies have however been confined to Newtonian flows. But industries related with fabrication of polymers and plastics at high temperatures show greater importance towards radiative flows of non-Newtonian fluids. The potential of non-Newtonian flows in ducts with radiative transfer were significantly developed after the studies on novel propellants for spacecraft [12]. The developments are extant and diversified the application of non-Newtonian fluid models. Most studies in this regard have employed the Rosseland model which is generally valid for optically-thick boundary layers. Recently, Kumar et al. [13] used such model to study melting heat transfer of hyperbolic tangent fluid over a stretching sheet with suspended dust particles. Cortell [14] and Batalle [15] have shown their earlier contribution towards radiative heat transfer of non-Newtonian fluids past stretching sheet under various circumstances. Relating to the studies Khan et al. [16] developed a numerical studies correlating MHD flow of Carreau fluid over a convectively heated surface with non-linear radiation. Appending to this studies Khan et al. [17] provided his results on hydromagnetic nonlinear thermally radiative nanoliquid flow with Newtonian heat along with mass conditions. Meanwhile, Rana and Bhargava [18] provided a numerical elucidation to study of heat transfer enhancement in mixed convection flow along a vertical plate with heat source/sink utilizing nanofluids. Hayat et al. [19] investigated the mixed convection stagnation-point flow of an incompressible non-Newtonian fluid over a stretching sheet under convective boundary conditions. Many diverse -physical simulations with and without convective and/or radiative heat transfer have been studied. Representative studies in this regard include [20–23] with analogous to the property of radiation flow.

Endeavoring the complications in three dimensional flow analysis, Shehzad et al. [24] studied the effect of thermal radiation in Jeffrey nanofluid by considering the characteristics of thermophoresis and Brownian motion for a solar energy model. Hayat et al. [25] analyzed the effect non-linear thermal radiation over MHD three-dimensional flow of couple stress nanofluid in the presence of thermophoresis and Brownian motion. Rudraswamy et al. [26] observations on Soret and Dufour effects in three-dimensional flow of Jeffery nanofluid in the presence of nonlinear thermal radiation clearly showed that concentration and associated boundary layer thickness are enhanced by increasing Soret and Dufour numbers. Many such problems [27–29] were considered disclosing the feature of thermal radiation in three dimensional flow of non-Newtonian fluids.

Inspired by the above works, we put forth the studies on the effect of non-linear thermal radiation on three dimensional flow of Carreau fluid with suspended nanoparticles. Present

http://dx.doi.org/10.5772/intechopen.76345

studies even include the phenomenon of mixed convection and convective boundary conditions. A numerical approach is provided for the above flow problem by employing Runge-Kutta-fourth-fifth order method.

2. Mathematical formulation

A steady three-dimensional flow of an incompressible Carreau fluid with suspended nano particles induced by bidirectional stretching surface at $z = 0$ has been considered. The sheet is aligned with the $xy-$ plane $(z = 0)$ and the flow takes place in the domain $z > 0$. Let $u = u_w(x) = ax$ and $v = v_w(y) = by$ be the velocities of the stretching sheet along x and y directions respectively. A constant magnetic field of strength B is applied in the $z-$ direction. Heat and mass transfer characteristics are taken in to account in the presence of Brownian motion and Thermophoresis effect. The thermo physical properties of fluid are taken to be constant.

Extra stress tensor for Carreau fluid is.

$$\overline{\tau}_{ij} = \mu_0 \left[1 + \frac{n-1}{2}\left(\Gamma\overline{\dot{\gamma}}\right)^2\right]\overline{\dot{\gamma}}_{ij}$$

In which $\overline{\tau}_{ij}$ is the extra stress tensor, μ_0 is the zero shear rate viscosity, Γ is the time constant, $\overline{\dot{\gamma}}$ is the power law index and is defined as.

$$\overline{\dot{\gamma}} = \sqrt{\frac{1}{2}\sum\sum\overline{\dot{\gamma}}_{ij}\overline{\dot{\gamma}}_{ji}} = \sqrt{\frac{1}{2}\Pi}$$

Here Π is the second invariant strain tensor.

The governing boundary layer equations of momentum, energy and concentration for three-dimensional flow of Carreau nanofluid can be written as,

$$\frac{\partial u}{\partial x} + \frac{\partial v}{\partial y} + \frac{\partial w}{\partial z} = 0, \tag{1}$$

$$u\frac{\partial u}{\partial x} + v\frac{\partial u}{\partial y} + w\frac{\partial u}{\partial z} = \nu\frac{\partial^2 u}{\partial z^2} + 3\frac{(n-1)}{2}\Gamma\left(\frac{\partial u}{\partial z}\right)^2\frac{\partial^2 u}{\partial z^2} + g\beta_T(T - T_\infty) - \frac{\sigma B^2}{\rho}u, \tag{2}$$

$$u\frac{\partial v}{\partial x} + v\frac{\partial v}{\partial y} + w\frac{\partial v}{\partial z} = \nu\frac{\partial^2 v}{\partial z^2} + 3\frac{(n-1)}{2}\Gamma\left(\frac{\partial v}{\partial z}\right)^2\frac{\partial^2 v}{\partial z^2} - \frac{\sigma B^2}{\rho}v, \tag{3}$$

$$u\frac{\partial T}{\partial x} + v\frac{\partial T}{\partial y} + w\frac{\partial T}{\partial z} = \alpha\frac{\partial^2 T}{\partial z^2} + \tau\left[D_B\frac{\partial T}{\partial z}\frac{\partial C}{\partial z} + \frac{D_T}{T_\infty}\left(\frac{\partial T}{\partial z}\right)^2\right] - \frac{1}{(\rho c)_f}\frac{\partial q_r}{\partial z}, \tag{4}$$

$$u\frac{\partial C}{\partial x} + v\frac{\partial C}{\partial y} + w\frac{\partial C}{\partial z} = D_B\frac{\partial^2 C}{\partial z^2} + \frac{D_T}{T_\infty}\frac{\partial^2 T}{\partial z^2}. \tag{5}$$

The boundary conditions for the present flow analysis are,

$$u = ax, v = by, w = 0, k\frac{\partial T}{\partial z} = -h_f\left(T_f - T_\infty\right), C = C_w \text{ at } z = 0 \tag{6}$$

$$u \to 0, v \to 0, T \to T_\infty, C \to C_\infty \text{ as } z \to \infty, \tag{7}$$

where ν is the kinematic viscosity of the fluid, μ is the coefficient of fluid viscosity, ρ is the fluid density, B is the magnetic field, σ is the electrical conductivity of the fluid, T is the fluid temperature, α is the thermal diffusivity of the fluid, k is the thermal conductivity. τ is the ratio of effective heat capacity of the nanoparticle material to heat capacity of the fluid, q_r is the radiative heat flux, g is the gravitational acceleration, β_T is thermal expansion coefficient of temperature, D_B is the Brownian diffusion coefficient, h_f is the heat transfer coefficient, D_T is the thermophoretic diffusion coefficient, c_p is the specific heat at constant pressure, T_f is the temperature at the wall, T_∞ is the temperatures far away from the surface. C is the concentration and C_∞ is the concentration far away from the surface. The subscript w denotes the wall condition.

Using the Rosseland approximation radiation heat flux q_r is simplified as,

$$q_r = -\frac{4\sigma^*}{3k^*}\frac{\partial T^4}{\partial z} = -\frac{16\sigma^*}{3k^*}T^3\frac{dT}{dz}, \tag{8}$$

where σ^* and k^* are the Stefan-Boltzmann constant and the mean absorption coefficient respectively.

In view to Eq. (8), Eq. (4) reduces to.

$$u\frac{\partial T}{\partial x} + v\frac{\partial T}{\partial y} + w\frac{\partial T}{\partial z} = \frac{\partial}{\partial z}\left[\left(\alpha + \frac{16\sigma^* T^3}{3k^*(\rho c)_f}\right)\frac{dT}{dz}\right] + \tau\left[D_B\frac{\partial T}{\partial z}\frac{\partial C}{\partial z} + \frac{D_T}{T_\infty}\left(\frac{\partial T}{\partial z}\right)^2\right]. \tag{9}$$

The momentum, energy and concentration equations can be transformed into the corresponding ordinary differential equations by the following similarity variables,

$$u = axf'(\eta), v = byg'(\eta), w = -\sqrt{a\nu}(f(\eta) + g(\eta)),$$
$$\theta(\eta) = \frac{T - T_\infty}{T_w - T_\infty}, \phi(\eta) = \frac{C - C_\infty}{C_w - C_\infty}, \eta = \sqrt{\frac{a}{\nu}} \tag{10}$$

where $T = T_\infty(1 + (\theta_w - 1)\theta(\eta)),\ \theta_w = \frac{T_f}{T_\infty},\ (\theta_w > 1)$ being the temperature ratio parameter.

Then, we can see that Eq. (1) is automatically satisfied, and Eqs. (2)–(7)are reduced to:

$$f''' + (f + g)f'' - f'^2 + 3\frac{n-1}{2}Wef''^2 f''' + \lambda\theta - Mf' = 0 \tag{11}$$

$$g''' + (f + g)g'' - g'^2 + 3\frac{n-1}{2}Weg''^2 g''' - Mg' = 0 \tag{12}$$

$$\frac{1}{\Pr}\left((1+R(\theta_w-1)\theta)^3\theta''\right)+(f+g)\theta'+Nb\theta'\varphi'+Nt\theta'^2=0, \tag{13}$$

$$\phi''+Le\Pr(f+g)\phi'+\frac{Nt}{Nb}\theta''=0 \tag{14}$$

With the boundary conditions,

$$f=0, g=0, f'=1, g'=c, \theta'=-Bi(1-\theta(0)),\ \ \phi=1,\ \text{ at }\ \eta=0,$$
$$f'\to 0, g'\to 0, \theta\to 0, \phi\to 0\ \text{ as }\ \eta\to\infty. \tag{15}$$

$We=\frac{c U_w^2\lambda^2}{\nu}$ is the Weissenberg number, $M=\frac{\sigma B^2}{\rho a}$ is the magnetic parameter, $c=\frac{b}{a}$ is the ratio of stretching rates, $\Pr=\frac{\nu}{\alpha}$ is Prandtl number, $R=\frac{16\sigma^* T_\infty^3}{3kk^*}$ is the radiation parameter, $Nb=\frac{\tau D_B(C_w-C_\infty)}{\nu}$ is the Brownian motion parameter, $Nt=\frac{\tau D_T\left(T_f-T_\infty\right)}{\nu T_\infty}$ is the Thermophoresis parameter, $\lambda=\frac{g\beta_T\left(T_f-T_\infty\right)}{\mathrm{Re}_x}$ is the mixed convection parameter, $Bi=\frac{h_f}{k}\sqrt{\frac{\nu}{a}}$ is the Biot number, $Le=\frac{\alpha}{D_B}$ is the Lewis number.

The local skin friction $\left(C_f\right)$, local Nusselt number (Nu_x) and local number Sherwood (Sh_x) are defined as,

$$C_{fx}=\frac{\tau_w}{\rho u_w(x)^2}, C_{fy}=\frac{\tau_w}{\rho v_w(y)^2}, Nu_x=\frac{u_w q_w}{ka\left(T_f-T_\infty\right)}\ \text{ and } Sh_x=\frac{u_w q_m}{D_B a(C_w-C_\infty)}$$

The local skin friction, local Nusselt number and Sherwood number is given by,

$$\sqrt{\mathrm{Re}_x}C_{fx}=\left[f''(0)+\frac{(n-1)We^2}{2}\left(f''(0)\right)^3\right],\quad \sqrt{\mathrm{Re}_x}C_{fy}=\left[g''(0)+\frac{(n-1)We^2}{2}\left(g''(0)\right)^3\right],$$

$$\frac{Nu_x}{\sqrt{\mathrm{Re}_x}}=-\left(1++R\theta_w^3\right)\theta'(0),\qquad \frac{Sh_x}{\sqrt{\mathrm{Re}_x}}=-\phi'(0).$$

where $\mathrm{Re}_x=\frac{u_w x}{\nu}$ is the local Reynolds number based on the stretching velocity. $u_w(x)$.

3. Numerical method

The non-linear ordinary differential Eqs. (11)–(14) subjected to boundary conditions (15) has been solved using the Runge-Kutta-Fehlberg fourth-fifth order method with the help of symbolic algebraic software MAPLE. The boundary conditions for $\eta=\infty$ are replaced by $f'\left(\eta_{\max}\right)=1, \theta\left(\eta_{\max}\right)=0$ and $\phi\left(\eta_{\max}\right)=0,$ where $\eta_{\max}$ is a sufficiently large value of η at which the boundary conditions (15) are satisfied. Thus, the values of $\eta=\eta_{\max}$ are taken to be 6. To validate the employed method, the authors have compared the results of $f''(0)$ and $g''(0)$

c	Wang [27]		Hayat et al. [30]		Present result	
	$-f''(0)$	$-g''(0)$	$-f''(0)$	$-g''(0)$	$-f''(0)$	$-g''(0)$
0	1	0	1	0	1	0
0.25	1.0488	0.1945	1.048810	0.19457	1.04881	0.19457
0.5	1.0930	0.4652	1.093095	0.465205	1.09309	0.46522
0.75	1.1344	0.7946	1.134500	0.794620	1.13450	0.79462
1.0	1.1737	1.1737	1.173721	1.173721	1.17372	1.17372

Table 1. Comparison of different values of c with Wang [27] and Hayat et al. [30].

with the that of published works by Wang [27] and Hayat [30] for the different values stretching parameter. These comparisons are given in **Table 1** and it shows that the results are in very good agreement.

4. Result and discussion

The purpose of this section is to analyze the effects of various physical parameters on the velocities, temperature and concentration fields. Therefore, for such objective, **Figures 1–11** has been plotted. Observations over these data with plotted graphs are discussed below.

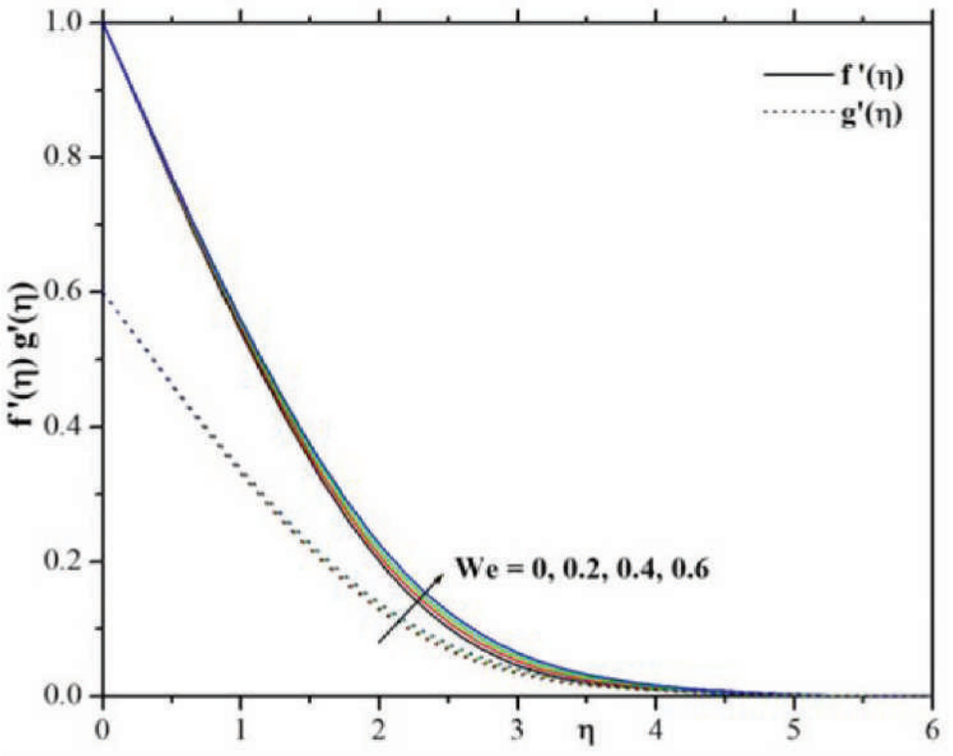

Figure 1. Influence of *We* on velocity profiles of both $f'(\eta)$ and $g'(\eta)$.

http://dx.doi.org/10.5772/intechopen.76345

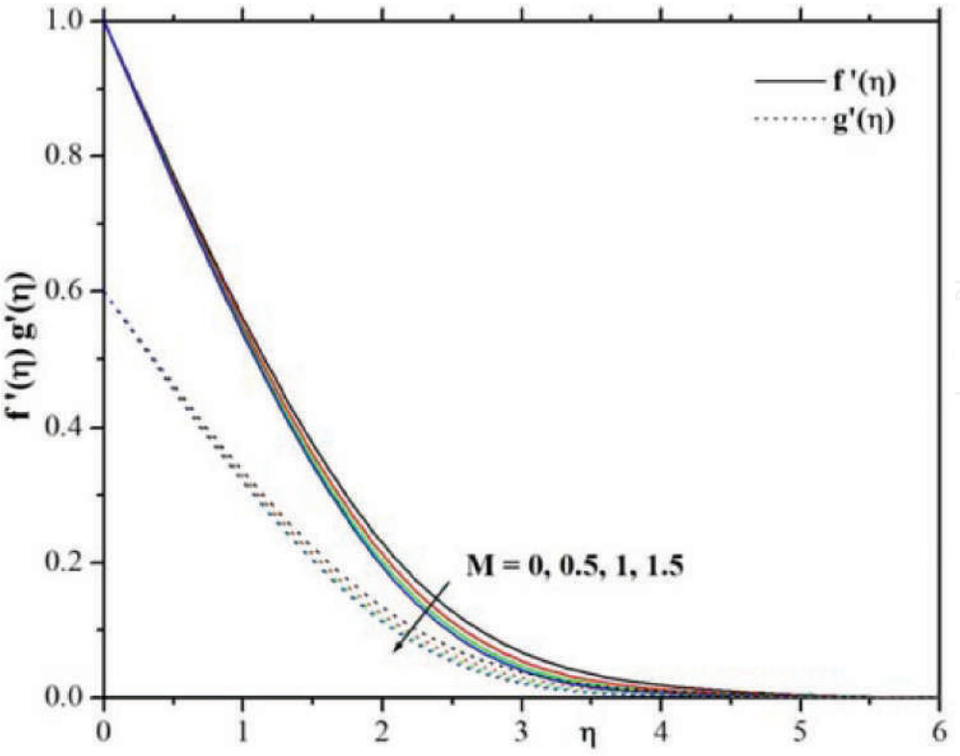

Figure 2. Influence of M on velocity profiles $f'(\eta)$ and $g'(\eta)$.

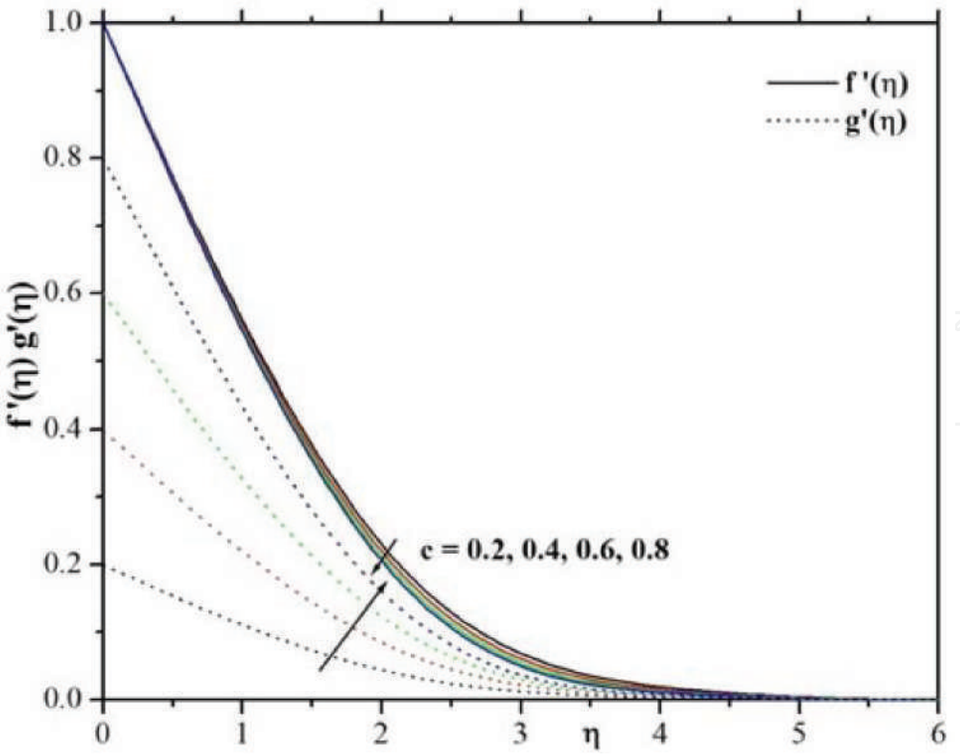

Figure 3. Influence of c on velocity profiles $f'(\eta)$ and $g'(\eta)$.

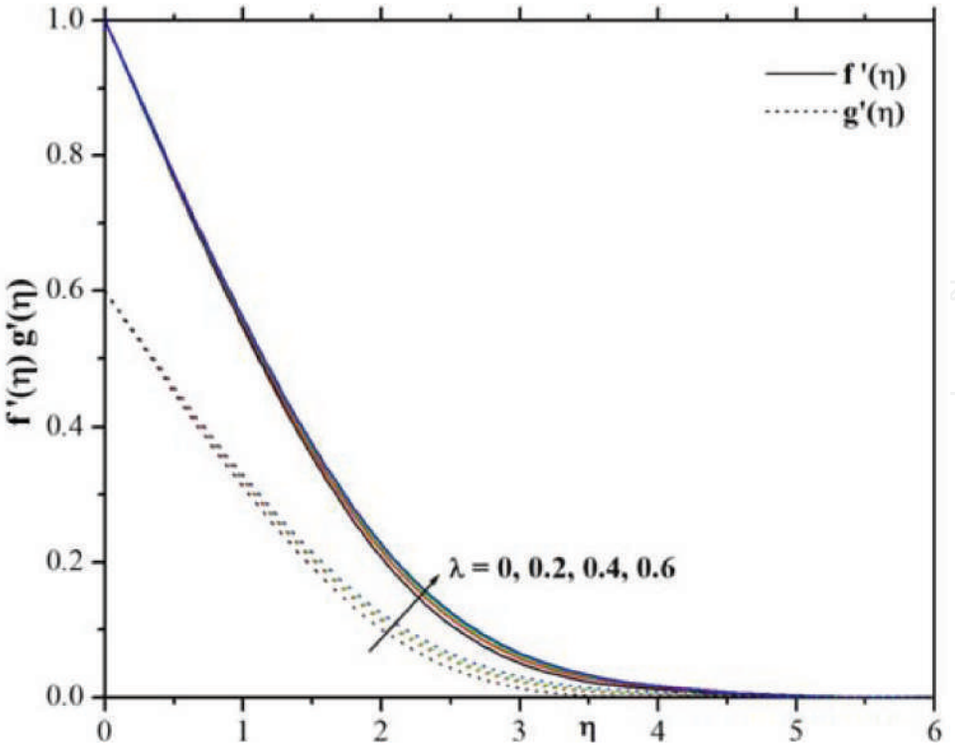

Figure 4. Influence of λ on velocity profiles $f'(\eta)$ and $g'(\eta)$.

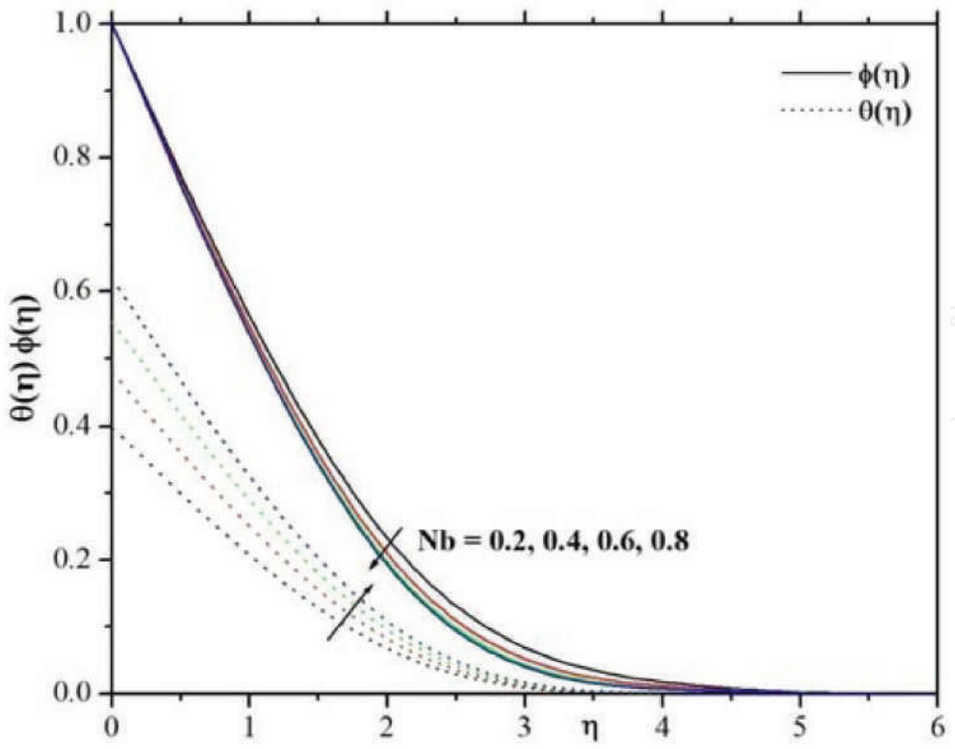

Figure 5. Influence of Nb on $\theta(\eta)$ and $\phi(\eta)$ profiles.

http://dx.doi.org/10.5772/intechopen.76345

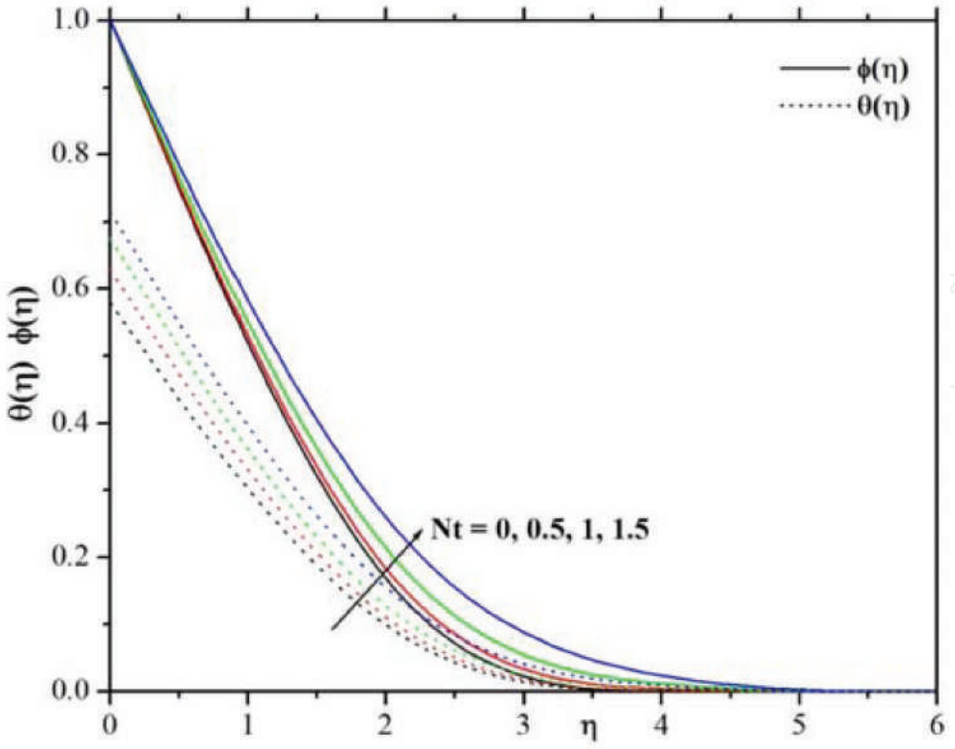

Figure 6. Influence of Nt on $\theta(\eta)$ and $\phi(\eta)$ profiles.

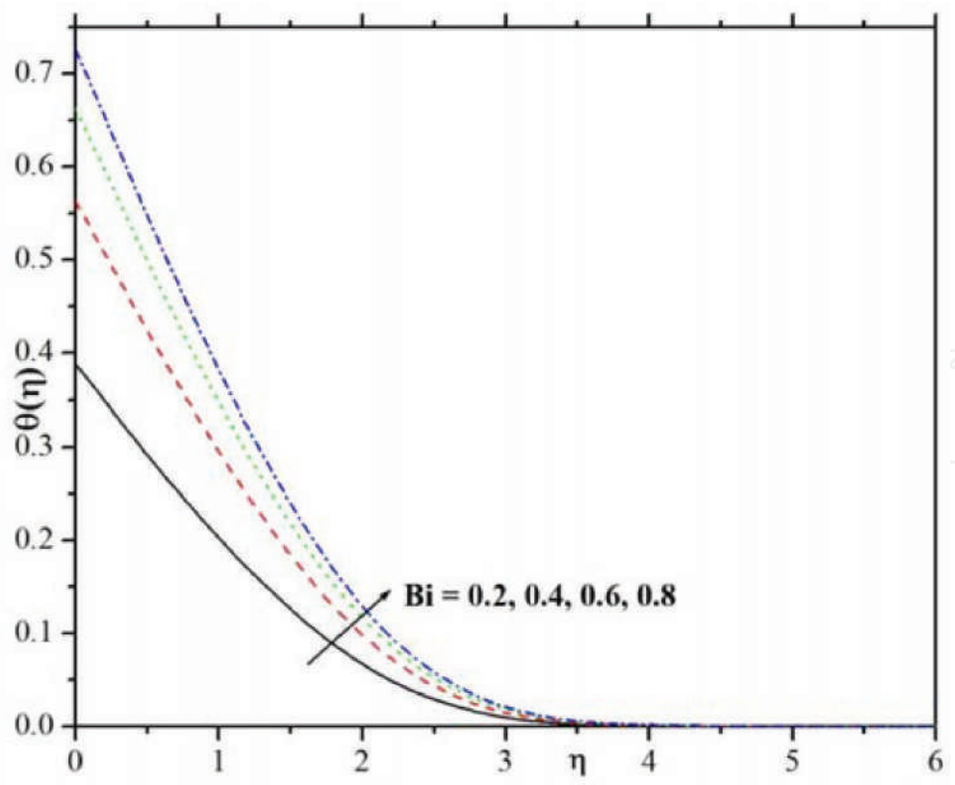

Figure 7. Influence of Bi on temperature profile.

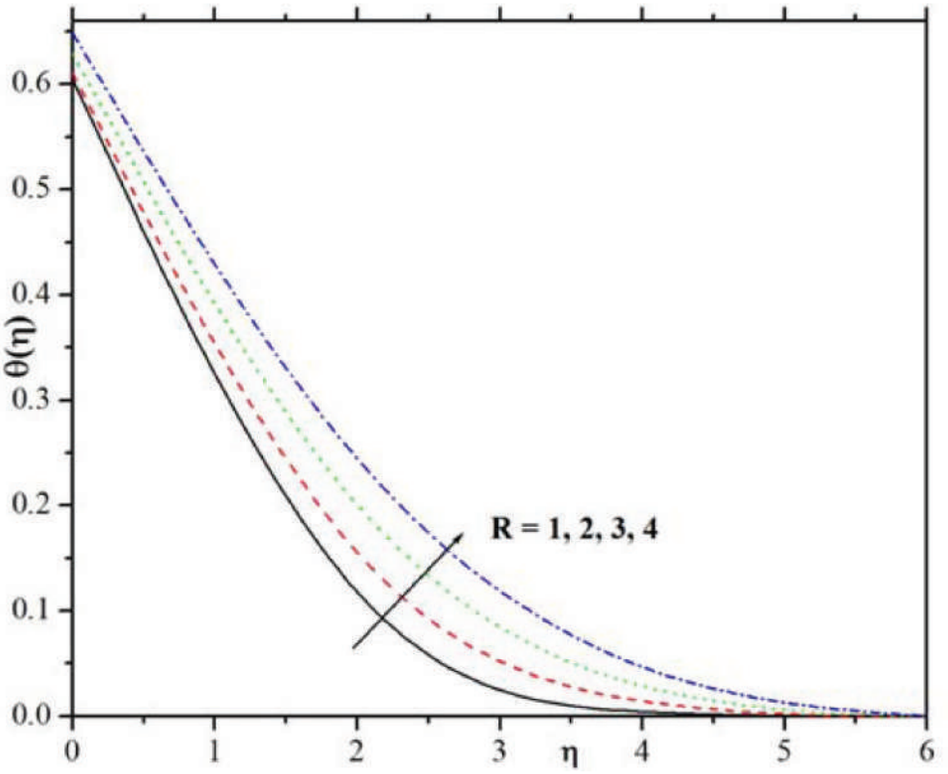

Figure 8. Influence of R on temperature profile.

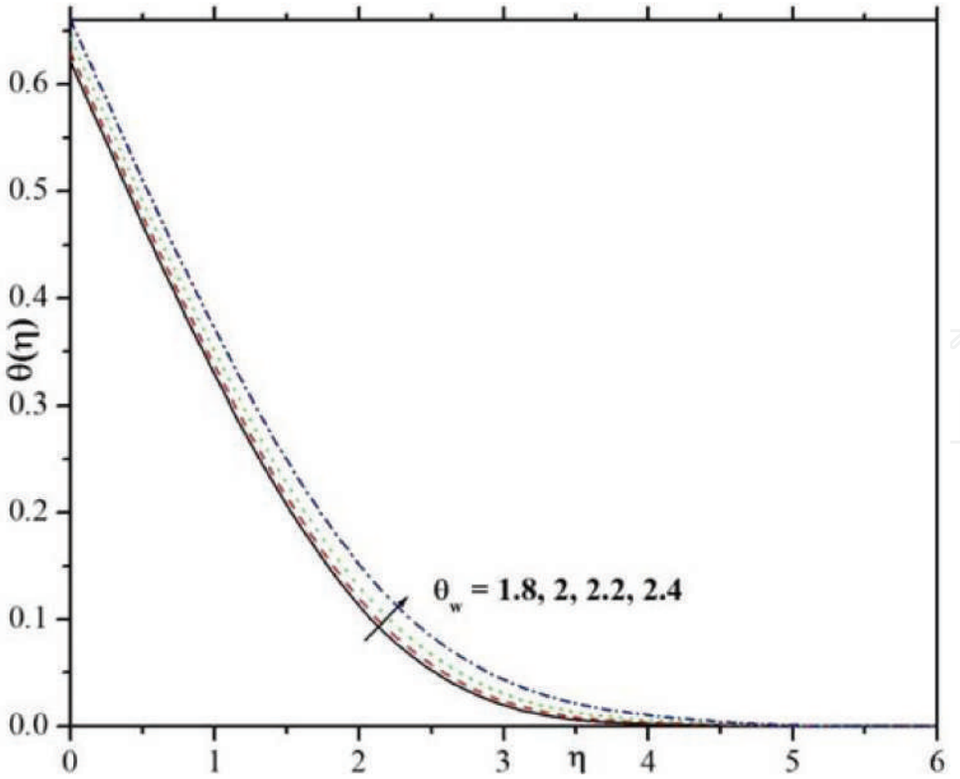

Figure 9. Influence of θ_w on temperature profile.

http://dx.doi.org/10.5772/intechopen.76345

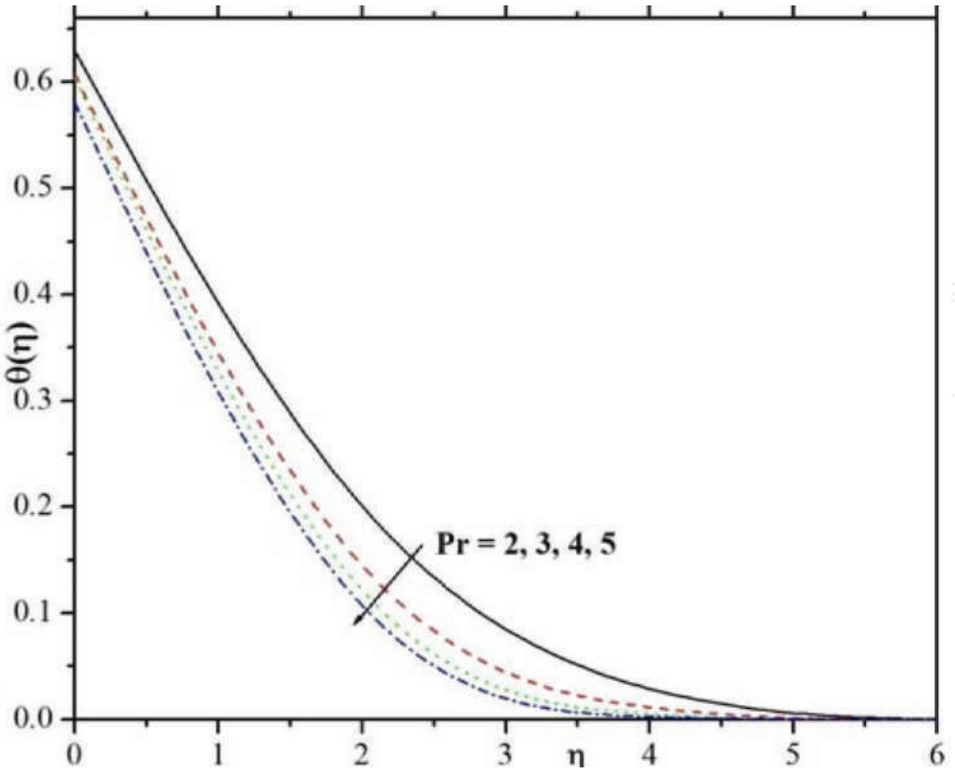

Figure 10. Influence of Pr on temperature profile.

Figure 1 characterizes the influence of Weissenberg number (We) on velocity profiles for both x and y direction. It is found that increasing values of the Weissenberg number increases the momentum boundary layers in both directions. Physically, Weissenberg number is directly proportional to the time constant and reciprocally proportional to the body. The time constant to body magnitude relation is higher for larger values of Weissenberg number. Hence, higher Weissenberg number causes to enhance the momentum boundary layer thickness.

The developments of a magnetic field (M) on velocity profiles are circulated in **Figure 2**. We tend to discover depreciation within the velocity profile for ascent values of magnetic field parameter. Physically, the drag force will increase with a rise within the magnetic flux and as a result, depreciation happens within the velocity field.

Figure 3 designed the velocity profiles of f' and g' for various values of stretching parameter(c). The velocity profiles and associated momentum boundary layer thickness decrease, once the stretching parameter will increase whereas velocity profile g′, exhibits the opposite behavior of f′. **Figure 4** shows the velocity profiles for different values of mixed convection parameter(λ). It depicts that the velocity field and momentum boundary layer thickness increases in both x and y direction by increasing mixed convection parameter.

Figure 5 portraits the consequences of Brownian motion parameter on temperature and concentration profile. The Brownian motion parameter (Nb) will increase the random motion of the fluid particles and thermal boundary layer thickness conjointly will increase which ends up

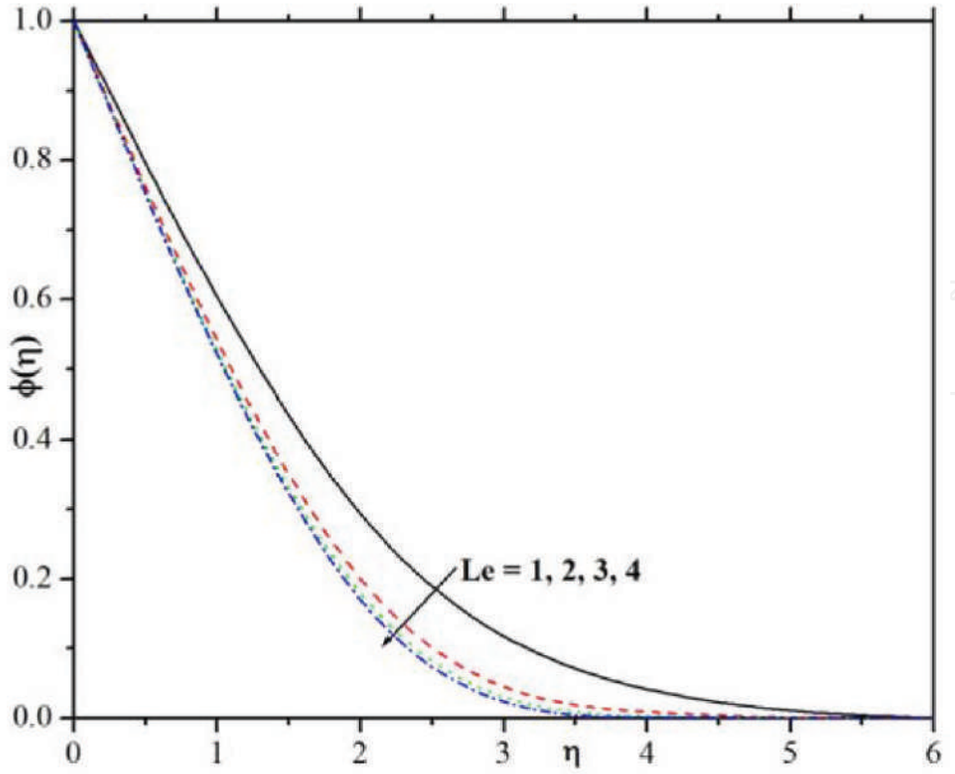

Figure 11. Influence of *Le* on concentration profile.

in an additional heat to provide. Therefore, temperature profile will increase however concentration profiles show opposite behavior.

The development of the thermophoresis parameter (Nt) on temperature and concentration profiles is inspecting in **Figure 6**. Form this figure we observed that, the higher values of thermophoresis parameter is to increases both $\theta(\eta)$ and $\phi(\eta)$ profiles. Further, the thermal boundary layer thickness is higher for larger values of thermophoresis parameter. This is because, it's a mechanism within which little particles area unit force off from the new surface to a chilly one. As a result, it maximizes the temperature and concentration of the fluid.

Figure 7 describe the influences of Biot number (Bi) on temperature profile. One can observe form the figure, the larger values of Biot number cause an enhancing the temperature profile. This is because, the stronger convection leads to the maximum surface temperatures which appreciably enhance the thermal boundary layer thickness.

Figures 8 and **9** are sketched to analyze the effect of radiation parameter (R) and temperature ratio (θ_w) parameter on temperature profile. The above graphs elucidate that, the temperature profile and thermal boundary layer thickness area unit increased by ascent values of radiation parameter and temperature ratio. Larger values of thermal radiation parameter provide more heat to working fluid that shows an enhancement in the temperature and thermal boundary layer thickness.

The effect of the Prandtl number (Pr) on $\theta(\eta)$ is seen in **Figure 10**. Since Pr is that the magnitude relation of the viscous diffusion rate to the thermal diffusion rate, the upper worth

Bi	*Le*	*R*	*c*	*λ*	*M*	**Absence**		**Presence**	
						C_{fx}	C_{fy}	C_{fx}	C_{fy}
0.2						1.2240	0.7261	1.3030	0.7836
0.4						1.1795	0.7280	1.2642	0.7847
0.6						1.1532	0.7289	1.2412	0.7854
	2					1.1719	0.7283	1.2575	0.7850
	3					1.1648	0.7285	1.2514	0.7851
	4					1.1619	0.7285	1.2489	0.7851
		1				1.1598	0.7289	1.2466	0.7855
		2				1.1420	0.7301	1.2300	0.7866
		3				1.1220	0.7314	1.2113	0.7878
			0.2			1.0852	0.2066	1.1657	0.2083
			0.4			1.1265	0.4509	1.2096	0.4657
			0.6			1.1648	0.7285	1.2514	0.7851
				0		1.3122	0.7242	1.3787	0.7816
				0.2		1.2523	0.7259	1.3143	0.7834
				0.4		1.1936	0.7276	1.2514	0.7851
					0	0.9611	0.5965	1.0281	0.6293
					0.5	1.1648	0.7285	1.2514	0.7851
					1	1.3441	0.8413	1.4521	0.9248

Table 2. Numerical result of skin friction coefficient for different physical parameter values for present and absence non Newtonian fluid.

of Prandtl number causes to scale back the thermal diffusivity. Consequently, for increasing values ofPr, the temperature profile gets decreases. The impact of Lewis number (Le) on nanoparticle concentration is plotted in **Figure 11**. It is evident that the larger values of Lewis number cause a reduction in nanoparticles concentration distribution. Lewis number depends on the Brownian diffusion coefficient. Higher Lewis number leads to the lower Brownian diffusion coefficient, which shows a weaker nanoparticle concentration.

Table 2 presents the numerical values of skin friction for various physical values in the presence and absence $(We = n = 0)$ of non-Newtonian fluid. It is observed that skin friction increase in both directions with increasing c for both presence and absence of non-Newtonian fluid. In the other hand, the skin friction coefficient decreases in both directions by increasingBi. The skin friction is higher in the presence of non-Newtonian fluid than in the absence of non-Newtonian fluid.

Table 3 also elucidates that, the wall temperature for different physical parameter for linear as well as nonlinear radiation. It reveals that, the wall temperature increases for increasing values of Bi, R and c for both linear and nonlinear radiation but the wall temperature decreases by

Bi	*Le*	*M*	*Nb*	*R*	*Nt*	Pr	*c*	Linear	Nonlinear
								$-\boldsymbol{Nu}_x(\mathbf{Re}_x)^{-1/2}$	$-Nu_x(\mathbf{Re}_x)^{-1/2}$
0.2								0.1060	0.3289
0.4								0.1356	0.4683
0.6								0.1479	0.5421
	2							0.1825	0.5501
	3							0.1428	0.5102
	4							0.1200	0.4886
		0						0.1440	0.5206
		0.5						0.1428	0.5102
		1						0.1418	0.5011
			0.2					0.3354	0.8074
			0.4					0.2771	0.6974
			0.6					0.2091	0.5974
				1				0.1768	0.8621
				2				0.2059	1.5030
				3				0.2150	2.0523
					0			0.1834	0.5641
					0.5			0.1331	0.4971
					1			0.0913	0.4351
						2		0.2165	0.4958
						3		0.2059	0.5260
						4		0.1875	0.5307
							0.2	0.1268	0.4606
							0.4	0.1352	0.4870
							0.6	0.1428	0.5102

Table 3. Numerical result of Nusselt number for different physical parameter values for linear and non nonlinear radiation.

increasing *Le, Nb, Nt* and Pr. Further, it is noticed that the wall temperature is higher for nonlinear radiation than that linear radiation.

Table 4 clearly shows the numerical values of skin friction, Nusselt number and Sherwood number for various physical parameters values. It reveals that, numerical values of wall temperature $\theta(0)$ increase by increasing *Bi*, θ_w, *R* and *c*. In the other hand Nusselt number decreases by increasing. *Le, M, Nb, Nt* and Pr. From this table, the skin friction coefficient increases by increasing *Bi* and *m*. Further, the Sherwood number increases by increasing *Bi*, θ_w, *R*, Pr and *We*.

Bi	θ_w	Le	M	Nb	R	Nt	Pr	We	c	λ	$-C_{fx}$	$-C_{fy}$	$-Sh_x(\mathrm{Re}_x)^{-1/2}$	$-Nu_x(\mathrm{Re}_x)^{-1/2}$
0.2											1.3030	0.7836	1.4859	0.3289
0.4											1.2642	0.7847	1.4877	0.4683
0.6											1.2412	0.7854	1.4886	0.5421
	1.8										1.2434	0.7856	1.4825	0.7398
	2										1.2353	0.7860	1.4812	0.9218
	2.2										1.2250	0.7865	1.4814	1.1226
		2									1.2575	0.7850	1.1427	0.5501
		3									1.2514	0.7851	1.4882	0.5102
		4									1.2489	0.7851	1.7744	0.4886
			0								1.0281	0.6293	1.5340	0.5206
			0.5								1.2514	0.7851	1.4882	0.5102
			1								1.4521	0.9248	1.4493	0.5011
				0.2							1.3140	0.7831	1.2408	0.8074
				0.4							1.2926	0.7837	1.4118	0.6974
				0.6							1.2713	0.7844	1.4647	0.5974
					1						1.2466	0.7855	1.4781	0.8621
					2						1.2300	0.7866	1.4727	1.5030
					3						1.2113	0.7878	1.4740	2.0523
						0					1.2674	0.7845	1.4869	0.5641
						0.5					1.2472	0.7853	1.4901	0.4971
						1					1.2255	0.7863	1.5060	0.4351
							2				1.2113	0.7878	1.4740	0.4958
							3				1.2345	0.7863	1.4731	0.5260
							4				1.2449	0.7857	1.4767	0.5307
								0			1.1936	0.7276	1.4746	0.5070
								1			1.2974	0.8329	1.4985	0.5127
								2			1.3712	0.9109	1.5141	0.5164
									0.2		1.1657	0.2083	1.2770	0.4606
									0.4		1.2096	0.4657	1.3862	0.4870
									0.6		1.2514	0.7851	1.4882	0.5102
										0	1.3787	0.7816	1.4738	0.5068
										0.2	1.3143	0.7834	1.4811	0.5085
										0.4	1.2514	0.7851	1.4882	0.5102

Table 4. Numerical result of local skin friction coefficient, Sherwood number and Nusselt number for different physical parameter.

5. Conclusions

In the present study, influence of nonlinear radiation on three dimensional flow of an incompressible non-Newtonian Carreau nanofluid has been obtained. The obtained results are presented in tabulated and graphical form with relevant discussion and the Major findings from this study are:

The velocity profiles increase in $x-$ directions and decrease in the $y-$ direction by increasing the stretching parameter.

Concentration profile increase by increasing the values *Nb* but in case of *Nt* concentration profile decreases.

Nb and *Nt* parameter shows the increasing behavior for temperature profile.

Effects of *Le* nanoparticle fraction $\phi(\eta)$ show the decreasing behavior.

Magnetic parameter reduces the velocity profiles in both x and $y-$ directions.

Temperature and thermal boundary layer thickness are decreased when the Pr and tl number increases.

Nonlinear thermal radiation should be kept low to use it as a coolant factor.

The rate of heat transfer increases with the increases in parameters *Rd* and θ_w.

We also noticed that the velocity profile and its associated boundary layer thickness are increases by increasing the values of *We*.

Author details

Rudraswamy N.G.[1]*, Ganeshkumar K.[2], Krishnamurthy M.R.[3], Gireesha B.J.[2] and Venkatesh P.[1]

*Address all correspondence to: ngrudraswamy@gmail.com

1 Department of Mathematics, Sahyadri Science College (Autonomous), Kuvempu University, Shimoga, India

2 Department of P.G. Studies and Research in Mathematics, Kuvempu University, Shankaraghatta, India

3 Department of Mathematics, JNN College of Engineering, Shivamogga, India

References

[1] Anwar Bég O, Ghosh SK, Narahari M, Bég TA. Mathematical modelling of thermal radiation effects on transient gravity-driven optically-thick gray convection flow along

an inclined plate with pressure gradient. Chemical Engineering Communications. 2011; **198**:1-15

[2] Rahman MM, Eltayeb IA. Radiative heat transfer in a hydromagnetic nanofluid past a non-linear stretching surface with convective boundary condition. Meccanica. 2013;**48**: 601-615

[3] Rashidi MM, Ganesh NV, Abdul Hakeem AK, Ganga B. Buoyancy effect on MHD flow of nanofluid over a stretching sheet in the presence of thermal radiation. Journal of Molecular Liquids. October 2014;**198**:234-238

[4] Srinivas S, Muthuraj R. Effects of thermal radiation and space porosity on MHD mixed convection flow in a vertical channel using homotopy analysis method. Communications in Nonlinear Science and Numerical Simulation. 2010;**15**:2098-2108

[5] Zeeshan A, Majeed A, Ellahi R. Effect of magnetic dipole on viscous ferro-fluid past a stretching surface with thermal radiation. Journal of Molecular Liquids. 2016;**215**:549-554

[6] Cortell R. Fluid flow and radiative nonlinear heat transfer over stretching sheet. Journal of King Saud University Science. 2013;**26**:161-167

[7] Ferdows M, Khan MS, Anwar Bég O, Azad MAK, Alam MM. Numerical study of transient magnetohydrodynamic radiative free convection nanofluid flow from a stretching permeable surface. Proceedings of Institution of Mechanical E-Part E: Journal of Process Mechanical Engineering. 2014;**228**(3):181-196

[8] Anwar Bég O, Ferdows M, Bég A, Tasveer T, Ahmed MW, Alam MM. Radiative optically-dense magnetized transient reactive transport phenomena with cross diffusion and dissipation effects. Numer. Simul. Journal of Taiwan Institute of Chemical Engineers. 2016:15

[9] Pal D, Mondal H. Effects of Soret Dufour, chemical reaction and thermal radiation on MHD non-Darcy unsteady mixed convective heat and mass transfer over a stretching sheet. Communications in Nonlinear Science and Numerical Simulation. 2011;**16**(4):1942-1958

[10] Murthy PVSN, Mukherjee S, Srinivasacharya D. Combined radiation and mixed convection from a vertical wall with suction/injection in a non–Darcy porous medium. Acta Mechanica. 2004;**168**(3–4):145

[11] Sheikholeslami M, Ganji DD, Javed MY, Ellahi R. Effect of thermal radiation on magnetohydrodynamics nanofluid flow and heat transfer by means of two phase model. Journal of Magnetism and Magnetic Materials. 2015;**374**:36-43

[12] S. Snyder, N. Arockiam, P.E. Sojka, Secondary Atomization of Elastic Non-Newtonian Liquid Drops, In: AIAA Joint Propulsion Conference, Nashville, Tennessee, USA, 2010

[13] Kumar KG, Gireesha BJ, Rudraswamy NG, Gorla RSR. Melting heat transfer of hyperbolic tangent fluid over a stretching sheet with fluid particle suspension and thermal radiation. Communications in Numerical Analysis. 2017;**2017**(2):125-140

[14] Cortell R. Effects of viscous dissipation and radiation on the thermal boundary layer over a nonlinearly stretching sheet. Physical Letters A. 2008;**372**(5):631-636

[15] Batalle RC. Viscoelastic fluid flow and heat transfer over a stretching sheet under the effects of a non-uniform heat source, viscous dissipation and thermal radiation. International Journal of Heat and Mass Transfer. 2007;**50**(15–16):3152-3162

[16] Khan M, Hussain M, Azam M. Magnetohydrodynamic flow of Carreau fluid over a convectively heated surface in the presence of non-linear radiation. JMMM. 2016;**412**:63-68

[17] Khan MI, Alsaedi A, Shehzad SA, Hayat T. Hydromagnetic nonlinear thermally radiative nanoliquid flow with Newtonian heat and mass conditions. Results Physics. 2017;**7**:2255-2260

[18] Rana P, Bhargava R. Numerical study of heat transfer enhancement in mixed convection flow along a vertical plate with heat source/sink utilizing nanofluids. Communication in Nonlinear Science Numerical Simulation. 2011;**16**(11):4318-4334

[19] Hayat T, Shehzad SA, Alsaedi A, Alhothuali MS. Mixed convection stagnation point flow of Casson fluid with convective boundary conditions. Chinese Physics Letters. 2012; **29**(11):114704. https://doi.org/10.1088/0256-307X/29/11/114704

[20] Laxmi T, Shankar B. Effect of nonlinear thermal radiation on boundary layer flow of viscous fluid over nonlinear stretching sheet with injection/suction. Journal of Applied Mathematical Physics. 2016;**4**:307-319

[21] Kumar KG, Rudraswamy NG, Gireesha BJ, Manjunatha S. Non-linear thermal radiation effect on Williamson fluid with particle-liquid suspension past a stretching surface. Results in Physics. 2017;**7**:3196-3202

[22] Kumar KG, Gireesha BJ, Manjunatha S, Rudraswamy NG. Effect of nonlinear thermal radiation on double-diffusive mixed convection boundary layer flow of viscoelastic nanofluid over a stretching sheet. International Journal of Mechanical Material Engineering. 2017;**12**(1):18

[23] Mabood F, Imtiaz M, Alsaedi A, Hayat T. Unsteady convective boundary layer flow of Maxwell fluid with nonlinear thermal radiation: A numerical study. International Journal of Nonlinear Science Numerical Simulation. 2016;**17**(5):221-229

[24] Shehzad SA, Hayat T, Alsaedi A, Obid MA. Nonlinear thermal radiation in three-dimensional flow of Jeffrey nanofluid: A model for solar energy. Applied Mathematics and Computation. 2016;**248**:273-286

[25] Hayat T, Muhammad T, Alsaedi A, Alhuthali MS. Magnetohydrodynamic three-dimensional flow of viscoelastic nanofluid in the presence of nonlinear thermal radiation. JMMM. 2015;**385**:222-229

[26] Rudraswamy NG, Kumar KG, Gireesha BJ, Gorla RSR. Soret and Dufour effects in three-dimensional flow of Jeffery nanofluid in the presence of nonlinear thermal radiation. Journal of Nanoengineering Nanomanufacturing. 2016;**6**(4):278-287

[27] Wang CY. The three-dimensional flow due to a stretching sheet. Physics of Fluids. 1984;**27**: 1915-1917

[28] Hayat T, Muhammad T, Shehzad SA, Alsaedi A. Similarity solution to three dimensional boundary layer flow of second grade nanofluid past a stretching surface with thermal radiation and heat source/sink. AIP Advances. 2015;**5**:017107. https://doi.org/10.1063/1.4905780

[29] Shehzad SA, Hayat T, Alsaedi A. MHD three dimensional flow of viscoelastic fluid with thermal radiation and variable thermal conductivity. A Journal of Central South University. 2014;**21**(10):3911-3917

[30] Hayat T, Shehzad SA, Alsaedi A. Three-dimensional stretched flow of Jeffrey fluid with variable thermal conductivity and thermal radiation. Applied Mathematics and Mechanics. 2013;**34**:823-832